Exploring the Accuracy of CFD Predictions for the Wake of a Hypersonic Inflatable Aerodynamic Decelerator

Clark Pederson* and Neil S. Rodrigues†
NASA Langley Research Center, Hampton, VA, 23681, USA

Hypersonic Inflatable Aerodynamic Decelerators (HIADs) present unique challenges that require accurate predictions of complex wake physics. This paper presents a comparative study between wind tunnel experiments and CFD simulations to investigate the wake velocities behind a simplified HIAD model at Mach 10. The CFD simulations were performed using unstructured meshes to capture the complex structure of both the wake and the flow around the sting. The experiments utilized planar laser-induced florescence (PLIF) to measure the off-body wake velocities in a non-intrusive manner. Modeling the turbulent fluctuations with steady Reynolds-averaged Navier-Stokes (RANS) models yielded large errors in wake velocities. Delayed Detached-Eddy Simulation (DDES) more accurately predicts the wake velocities near the body and captured the same trends as experiments with increasing Reynolds number. However, DDES had difficulty predicting the shear layers near separation, underpredicting the shear layer thickness. The sensitivity of the hybrid RANS/LES results to the mesh resolution are also demonstrated.

Nomenclature

D	The maximum diameter
k	Turbulent kinetic energy
M_∞	Freestream Mach number
Q	Q-criterion
Re_D	Reynolds number based on the maximum diameter and the freestream conditions
T_∞	Freestream temperature
U_∞	Freestream velocity
x	Axial coordinate, parallel with the centerline
y	Transverse coordinate, perpendicular to the centerline
Δ	Cell size
Δt	Physical timestep
μ_t	Turbulent eddy viscosity
ω	Vorticity vector

I. Introduction

The proper design of entry, descent, and landing vehicles requires accurate predictions of the extreme heating experienced during atmospheric entry. New challenges in both planetary missions and earth re-entry will require both innovative heatshield technologies and more accurate flow predictions. For example, human exploration of Mars will require significantly larger payloads than previously delivered for the Mars Science Laboratory or Mars2020 missions [1]. Due to the thin atmosphere of Mars, achieving sufficient drag to slow down the large payloads will require novel lander vehicles. For a given payload, a larger heatshield diameter yields lower peak heating and higher drag. Unfortunately, the maximum heatshield diameter is often limited by the launch vehicle fairing size. This difficulty motivates the development of Hypersonic Inflatable Aerodynamic Decelerators (HIADs) [2]. A HIAD is a soft-goods aeroshell that can be compactly stored inside the payload shroud of a launch vehicle during launch and cruise, then inflated to its

*Aerothermodynamics Branch, AIAA Member
†Optical Physicist, Advanced Measurements and Data Systems Branch, AIAA Senior Member

maximum diameter prior to atmospheric entry. This expansion allows for larger vehicle diameters without requiring launch vehicles with larger fairings. The most recent flight test of a HIAD was the Low-earth Orbit Flight-Test of an Inflatable Decelerator (LOFTID), which successfully completed on November 10th, 2022 [3]. A cross-section of the LOFTID vehicle is shown in Fig. 1.

The success of LOFTID has spurred additional interest in HIADs for Mars missions, earth reentry, and launch asset recovery. These new missions will require accurate predictions of the wake region. Unlike the Orion crew module or the Mars2020 lander, HIADs have an exposed backshell with minimal thermal protection systems. Protecting the inflatable toroids, straps, and payload requires accurate heat flux predictions with low uncertainty. The difficulties with wake heating will become more significant on future missions with larger payloads and higher entry velocities, including human missions. Both LOFTID flight measurements and wind tunnel tests provide data that can be used to enhance the accuracy of computational fluid dynamics (CFD) in predicting these hypersonic wakes.

Predicting the wake of a supersonic vehicle has remained a consistent challenge for many decades. Campbell and Brown [4] described "extreme difficulties" modeling the wake pressure for Viking landers. Compressibility dramatically reduces the thickness of turbulent shear layers, including the shear layers that envelop the wake. Conventional steady Reynolds-averaged Navier-Stokes (RANS) models fail to correctly predict this decrease in thickness. Predicting the thickness and the corresponding Reynolds stress are important to predicting the expansion that occurs around the shoulder and into the wake of a blunt-body vehicle. Compressibility corrections have been proposed, e.g. the corrections by Wilcox [5, 6], but these predictions are ad hoc in nature and do not generalize well to flows with attached boundary layers [7]. In a recent validation study of a Mars entry vehicle [8], the compressibility correction by Spalart [9] yielded some improvement in wake predictions of drag, but still left large unphysical variations in wake pressure.

Scale-resolving simulations have emerged as a way to obtain higher fidelity in wake flow simulations, albeit at a higher computational cost than steady RANS models. While steady RANS simulations only resolve the average state of a flow, scale-resolving simulations use a time-accurate simulation to directly represent some of the unsteady turbulent fluctuations. Scale-resolving simulations include large-eddy simulations (LES), where the majority of the turbulent fluctuations are directly represented and a subgrid model is used in modeling the effect of the unresolved scales on the resolved scales. LES is costly for wall-bounded flows due to the presence of very small eddies near the wall, leading to efforts to model the effects of the near-wall eddies on the external flow. One approach is a hybrid RANS/LES (HRLES) model: steady RANS is used where its predictions are accurate, such as attached boundary layers, while LES is used where higher fidelity is required. Common examples of HRLES models are Detached-Eddy Simulation (DES) [10, 11] and Delayed Detached-Eddy Simulation (DDES) [12]. More details can be found in the review papers by Fröhlich and von Terzi [13] and Heinz [14]. Several studies have demonstrated that HRLES can be used to accurately predict wake pressures [15–17] and wake heating [17, 18] in supersonic flow. Additionally, Sinha and Candler [19] studied a reentry vehicle at transitional Reynolds numbers and suggested that DES can approach laminar behavior if given sufficient grid resolution.

The successes of scale-resolving simulations lead to the current validation effort, focused on the wake of a HIAD. CFD validation requires carefully designed experiments; a simple comparison of integrated loads can fail to discriminate between accurate and inaccurate physical models. Error cancellations can lead to the mistaken belief that a model is performing well when it has large errors. For example, Schwing and Candler [20] demonstrated that DES simulations of a reentry crew module could match the experimental data for integrated aerodynamic coefficients, while giving poor predictions of the surface pressure distributions. Non-intrusive measurements of velocity fields provide a much better understanding of the flow structures and key physics. Wake measurements can clearly show when a wake simulation has large errors; for example, differences in grid resolution and turbulence models can change the length of the recirculation

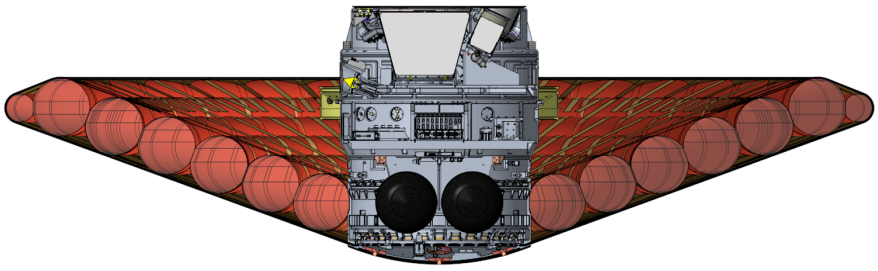

Fig. 1 Cross-section of the LOFTID flight vehicle.

region by as much as 100%. For these reasons, the recent experiments by Rodrigues et al. [21, 22] on a LOFTID geometry are a valuable dataset for CFD validation.

The present work explores higher Mach numbers than many previous validation studies of supersonic wakes. Numerous experimental and computational studies have been conducted on supersonic axisymmetric wakes at Mach 2 to 4, such as Refs. [23–25]. In comparison, the current study has a freestream Mach number of 10. The current study also combines a complex, flight-relevant geometry with non-intrusive velocimetry. Many studies on flight-relevant vehicle geometries are limited to only integrated forces or surface pressures. These quantities are useful for engineering design, but they provide limited ability to assess the impact of modeling decisions on the flowfield as a whole. Planar velocimetry like that by Rodrigues et al. [21, 22] provides a more rich and discriminating set of CFD validation data.

The primary focus of this paper is a critical evaluation of the accuracy of unstructured finite-volume CFD in predicting the wake velocities of a HIAD at Mach 10. First, a brief summary of the flowfield and associated physics is presented in Section II. The computational tools used for the validation is described in Section III. The experimental campaign by Rodrigues et al. [21, 21] will be summarized in Section IV. Finally, the CFD results are compared with experimental data in Section V.

II. Wake Flow Description

Hypersonic wake flows involve a complex array of physical phenomenon, as shown in Fig. 2. A bow shock forms at the front of a blunt body, with a stagnation point flow directly behind. A separated flow forms in the wake with the separation point near the maximum diameter. An expansion fan forms around the shoulder of the vehicle, turning the streamlines toward the centerline axis. A recirculation region with subsonic flow forms immediately behind the vehicle and is surrounded by a detached shear layer that may be laminar, transitional, or turbulent depending on the Reynolds number. At some distance downstream, the flow turns through a recompression shock to align with the axis of the vehicle. The physics of supersonic wakes has been studied experimentally, such as in Ref. [23, 25], revealing complex physics which are less understood than incompressible, subsonic wakes. In this validation campaign, a sting was used to support the model, as shown in Fig. 2. This sting has a significant impact on the wake dynamics and is therefore included in the simulations. The validation effort focuses on velocities along a z-normal plane on the model centerline so that the sting does not directly impede the measurements. This slice and the associated flow are illustrated in Fig. 3.

While the current validation effort focuses specifically on the velocities in the wake, the size of the recirculation region is closely related to the surface pressure and heating. The flow expands from high to low pressure as it turns around the shoulder of the vehicle; a smaller reciruclation region will result in a lower pressure and higher heating at the surface. Additionally, smaller recirculation regions with stronger reverse velocities show larger variations in heating and pressure across the separated region. Predicting the correct extent of the recirculation region is necessary to accurately predict engineering quantities of interest at the surface.

There are several factors which limit the magnitude of the unsteadiness behind a LOFTID vehicle at higher Mach numbers. First, the Reynolds number is relatively low both during flight and in the reported experimental campaigns. This means the forebody boundary layers and detached shear layers are often transitional instead of fully turbulent. Second, a sting damps the wake unsteadiness, even when the wake is offset from the centerline [26]. Third, compressibility effects limit the growth of Kelvin-Helmholtz instabilities, as seen in early experimental and numerical campaigns studying compressible mixing layers [27]. These effects lead to relatively weak instabilities and slow growth of the detached shear layers, at least compared to an incompressible analog.

The simulations and the corresponding measurements were obtained at three different freestream conditions, labeled here as "Low," "Mid," and "High" Reynolds numbers. The freestream density, velocity, and temperature for these three conditions are reported in Table 1. These boundary conditions were used for the simulations to match the reported experimental wind tunnel conditions. There are slight differences between the calculated Mach and Reynolds numbers in the experiment and the simulations, which are due to slight differences in the specific gas constant and viscosity model. When reporting conditions, the experiment uses a Chapman-Cowling relationship for the viscosity and a virial equation of state with a compressibility factor, as described by Hollis [28]. The computations used an ideal gas law with no compressibility factor and a Sutherland viscosity law with coefficients of $\mu_0 = 1.716 \times 10^{-5}\,\mathrm{kg\,m^{-1}\,s^{-1}}$, $T_0 = 273.15\,\mathrm{K}$, and $S = 110.4\,\mathrm{K}$. The experimental Reynolds numbers reported by Rodrigues et al. [22] are $Re_D = 2.3 \times 10^5$, 4.5×10^5, and 7.9×10^5.

The exact onset of transition is not clear from the experimental data. The instantaneous snapshots, as shown in Fig. 4 show a range of scales that suggest turbulent flow in some portion of the wake. However, experiments at Mach 10 on similar 70-degree sphere show that the boundary layer on the heat shield remained laminar until $Re_D \approx 7E6$ [29].

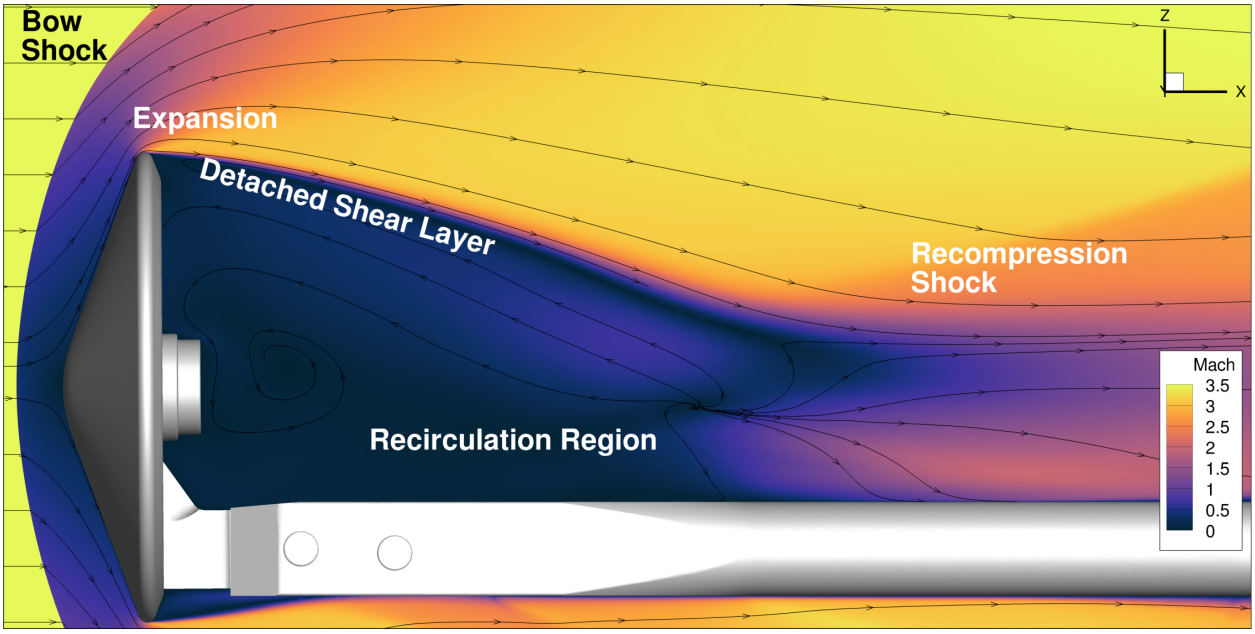

Fig. 2 Illustration of the flow features in the wake of the LOFTID PLIF test article, using a slice taken along the y-normal symmetry plane. The incoming flow is at Mach 9.9 and $Re_D = 8.9 \times 10^5$.

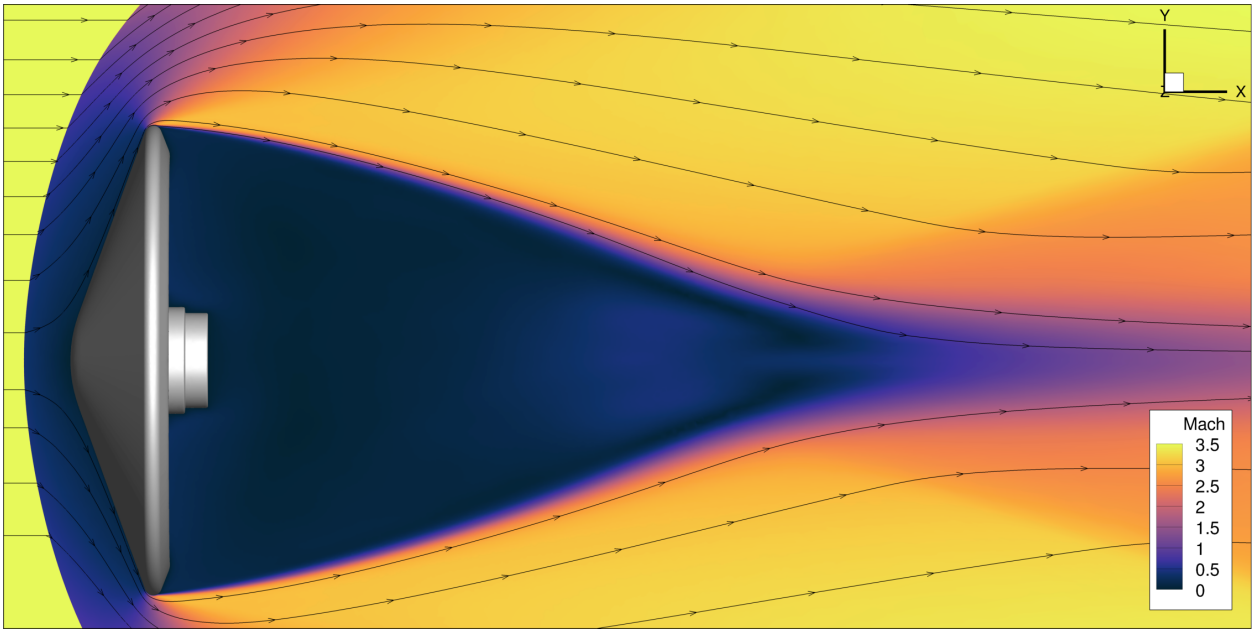

Fig. 3 Illustration of the wake of the LOFTID PLIF test article using a slice taken on a z-normal plane at the centerline. This is the same plane on which PLIF measurements were taken. The incoming flow is at Mach 9.9 and $Re_D = 8.9 \times 10^5$.

Table 1 Wind tunnel conditions

Tag	$Re_{D,\infty}$	M_∞	ρ_∞ [kg/m3]	u_∞ [m/s]	T_∞ [K]
Low Re	2.51e+05	9.68	4.68e-03	1385	50.9
Mid Re	5.03e+05	9.81	9.13e-03	1386	49.7
High Re	8.93e+05	9.91	1.58e-02	1387	48.7

For the Reynolds numbers considered in this experiment, the boundary layer is most likely laminar or transitional as it approaches the separation point.

III. Computational Approach

This study uses two codes produced by NASA Langley Research Center: FUN3D [30] and HyperSolve [31, 32]. These two codes use the finite-volume method to solve the Favre-averaged Navier-Stokes equations.

- **FUN3D** uses a node-based, dual-mesh discretization. For steady calculations, the inviscid fluxes were discretized by using a dissipative LDFSS scheme [33]. For the unsteady calculations, the inviscid fluxes were discretized with a modified Roe scheme with lower dissipation in subsonic regions [34]. Stencil-based Van Albada limiters are used. The viscous fluxes were discretized by using Green-Gauss element-based gradients, which is equivalent to a Galerkin-based approach for regular tetrahedra.
- **HyperSolve** uses a node-centered, edge-based finite volume discretization. The inviscid fluxes are discretized by using an edge-based Roe scheme with reconstruction. Similar to FUN3D, a low-dissipation Roe scheme is used for the unsteady calculations [34]. A pressure-based limiter by Gnoffo and White [35] is used. The viscous fluxes are discretized with the alpha-damping scheme by Nishikawa et al. [36, 37] and $\alpha = 1$. HyperSolve also employs a Jacobian-Free Newton-Krylov (JFNK) solver to solve the linear systems efficiently and robustly.

Section V.D includes a comparison of the results from the two flow solvers. In general, predictions between the two solvers agreed well.

Because the wake is unsteady, two different solution strategies were explored: For the first strategy, a steady solution was obtained using local time-stepping. Machine-zero convergence of the residual was difficult to achieve to due to the low-Mach unsteadiness in the wake. The simulations were stopped after decreasing the residuals by eight orders of magnitude. The second strategy was to perform unsteady DDES calculations, which directly resolve some of the turbulent fluctuations and only model the unresolved turbulent fluctuations. The unsteady solution was time-averaged for comparison with experimental values of mean velocity. A BDF2 scheme was used with dual-time-stepping for the time integration. Ten dual time-steps were used for each physical time-step, which was sufficient to decrease the unsteady residual by two orders of magnitude. Using more dual-timesteps to obtain smaller temporal errors was not observed to have any significant impact on the mean or RMS velocity fields. The physical timesteps were set to acheive a CFL of 1 or less through most of the recirculating wake region; this led to a timestep of $\Delta t U_\infty/\Delta \approx 4$, where Δ is the cell size in the wake. A startup period of 2000 iterations was used to initialize the unsteady solution on each mesh. After that, the simulations were run for a period of $240D/U_\infty$ while collecting time-averaged data; for a coarse mesh where $\Delta/D \approx 1\%$, this was 8000 iterations.

For the higher Reynolds numbers, the wake in the experiments is transitional or fully turbulent. Therefore, a turbulence model is necessary to model the unresolved turbulent fluctuations. Several different turbulence models were examined, including both steady RANS and HRLES models. This paper uses the nomenclature established by the Turbulence Modeling Resource [38] for describing the various turbulence models. The following models were tested:

- **SA-neg**: This is a one-equation Spalart-Allmaras model by Allmaras et al. [39]. For converged solutions on fine grids, it is identical to the original Spalart Allmaras model [40].
- **SA-neg-RC**: This is a one-equation Spalart-Allmaras model by Allmaras et al. [39] with a Rotation/Curvature correction [41].
- **SST-Vm**: This is a variant of the Shear Stress Transport model by Menter et al. [42]. This common variant has several changes to the published version: the isotropic part with k is omitted from the Reynolds stress model when it appears in the momentum and energy equations, and the production term is replaced by $\mu_t \Omega^2$, where Ω is the magnitude of the vorticity vector.
- **DDES**: This is a HRLES method published by Spalart [12], known as Delayed Detached-Eddy Simulation. The

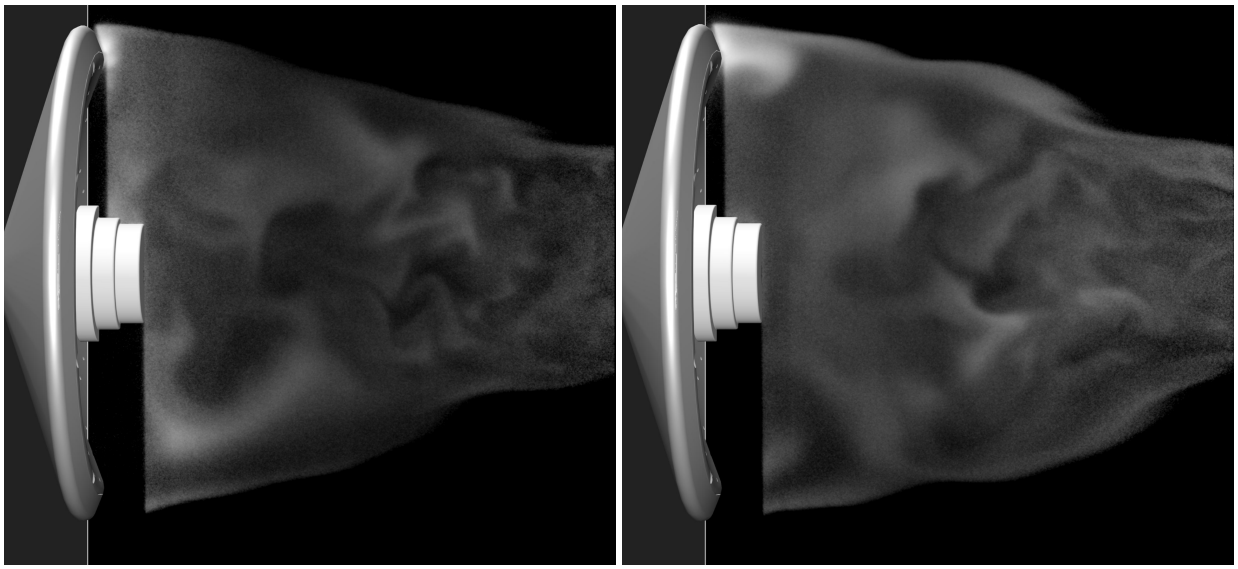

Fig. 4 Example instantaneous snapshots from the PLIF experiments at the higher Reynolds number. The PLIF signal intensity is shown with a logarithmic scale. More PLIF snapshots are in Ref. [22]

SA-neg-RC model was used as the underlying RANS model for DDES.

These turbulence models were run as "fully turbulent," meaning that the source terms were not modified to manually specify a transition location. As shown by Rumsey [43], both SA-neg and SST models allow a stable, laminar solution with negligible eddy viscosity at low Reynolds numbers. In the current work, the turbulence models do show laminar behavior over most of the boundary layer on the heatshield, even though the turbulence models are used everywhere.

There are a wide variety of RANS turbulence models with varying accuracy. A brief discussion of the varying accuracy of different turbulence models is included in the Appendix. It is possible that models such as the Wilcox 2006 model [5] outperform the RANS models examined in this study. However, current RANS models seem fundamentally limited in their ability to capture compressible shear layers and supersonic wakes. In previous studies of supersonic wakes at Mach 1.4 [20] and Mach 2.5 [15], RANS models gave poor predictions of the wake pressure and the recirculation length. This paper considers much higher Mach numbers than the previous validation studies, but the errors seen with RANS are consistent with those seen in previous studies. HRLES models were seen as a more productive area for research.

A. Mesh for Steady Simulations

Grid generation is an important part of CFD, and high-quality solutions usually require high-quality grids. "High quality" can be defined in several ways for the wake of a blunt-body vehicle. First, the mesh should be tailored to the bow shock to minimize numerical errors. As shown by Candler et al. [44] and McCloud [45], large, misaligned cells near a bow shock can have significant impacts on overall solution accuracy. Second, the grid must be fine enough to resolve any gradients in the solution that will impact the quantities of interest, including boundary layers and isentropic expansions. Finally, the boundary layer should have a relatively fine wall-normal spacing to resolve the viscous sublayer.

While many previous studies of supersonic wakes have used manually crafted meshes, the geometry in the current study is more complex than a simple cylinder or an Apollo-style capsule. The test article, shown in Fig. 8a, includes a concave backshell and a representative payload. Even though an offset sting was used, the sting will still impact the wake dynamics and was included in the computational domain. These geometric details make manual crafting of meshes laborious and error-prone. To help create high-quality meshes for a complex geometry, this paper makes use of the Sketch-to-Solution (S2S) process [46]. S2S is an iterative process where anisotropic unstructured adaptation is used to convert an initial coarse mesh to a high-quality fine mesh. The S2S workflow is pictured in Fig. 5. An initial mesh is generated, and an initial (inaccurate) solution is obtained on the initial mesh. The mesh resolution is measured by the complexity, as defined by Alauzet et al. [47]. For practical use, the complexity is proportional to the number of nodes. The mesh is iteratively adapted and refined using the software tool *refine*, with several adaptation cycles occurring at a

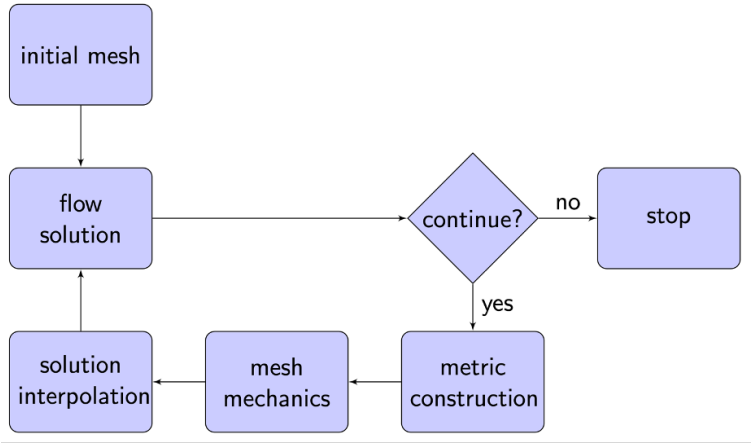

Fig. 5 Grid adaptation process when using S2S

given mesh complexity before increasing the resolution. Usually, the cycle of adaptation and refinement is continued until a predefined complexity limit is reached.

The S2S process can be used with multiscale metric adaptation. Multiscale mesh adaptation attempts to minimize the L_2 norm of the interpolation error of a scalar field such as temperature or Mach number. After running the CFD solver and generating an output scalar field, the Hessian of the target scalar field is calculated. This Hessian is then decomposed into eigenvalues and eigenvectors. A Riemannian metric tensor is formed by recombining the inverse square of the eigenvalues with the eigenvectors to ensure a symmetric, positive-definite metric; the metric is then used to construct an anisotropic grid. For further details on multiscale metric adaptation, see Refs. [47–49].

An example slice of the adapted mesh is shown in Fig. 6; the mesh shown has 2.3 million nodes. The mesh is adapted to give a high mesh density and crisp resolution around the bow shock. A high grid density is seen at the expansion fan around the shoulder and the wake shear layer. Anisotropic, highly stretched cells appear in the far wake, where the axial velocity gradients are relatively smooth.

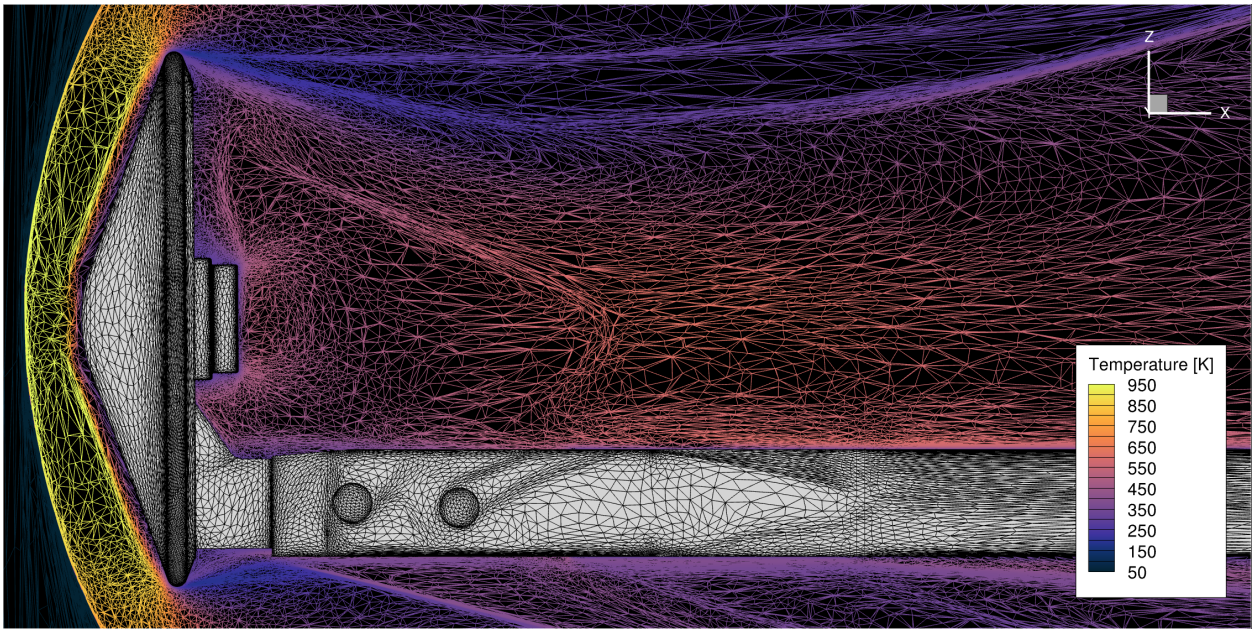

Fig. 6 A slice through the symmetry plane of an adapted mesh, generated using Sketch-to-Solution. The conditions correspond to the $Re_D = 2.5 \times 10^5$case. The mesh is colored by the temperature to show the flow features to which grid is adapted.

B. Mesh for Unsteady Simulations

Creating a high-quality mesh for an unsteady DDES simulation places extra grid requirements. Spalart [50] suggested dividing the mesh into near-wall RANS regions and a "focus region" in the wake with isotropic, fine cells. The focus region is the portion of the domain where the mesh is fine enough to directly resolve LES-type turbulent fluctuations. A wake resolution of $\Delta/D \approx 1\%$ is common for HRLES of supersonic wakes [17, 19, 20, 51].

The multiscale metric adaptation that is common in RANS has limited capability to capture unsteady wakes. The mean flow can be relatively smooth in wakes, leading to coarse resolution precisely where extra resolution is needed. This can be seen in Fig. 7a, where the wake spacing is quite large. The fixed-point iteration of Alauzet et al. [52] was attempted in an attempt to apply the multiscale-metric adaptation to a transient metric field. Unfortunately, the fixed-point iteration did not yield a fine wake resolution until very high node counts; this difficulty was also noticed in the paper by Park et al. [53]. Instead of fixed-point iteration, this paper uses an approach similar to that proposed by Ekelschot and Brock [54]: The starting point is the fine-mesh from a steady SA-neg simulation. The metric field is then modified to place an upper limiter of a fixed Δ spacing in the wake region from $x/D = 0.28$ to $x/D = 1.18$. Various mesh spacings were examined, as shown in Fig. 7 and Table. 3. Most of the DDES results in this paper used a medium resolution of $\Delta/D \approx 0.5\%$. Section V.C shows comparisons on coarser and finer meshes for the higher Reynolds number case. For the coarse and medium DDES meshes, the minimum edge length of a cell was set to 0.25 times the upper limit, effectively limiting the aspect ratio to four. Purely isotropic cell spacings in the wake region were compared; the mean velocity only showed small differences. The wake region was blended with the existing RANS metric field using an exponential decay.

For these DDES meshes, no further adaptation cycles were used to improve on the initial DDES mesh. The regions that use the anisotropic multiscale metric are generally steady, and the solution does not change significantly due to the improved wake resolution. Conversely, the solution in the wake does change, but the mesh in this region is defined by the fixed isotropic spacing and is not dependent on the solution.

IV. Experimental Setup

A wind tunnel test using PLIF was performed on a representative LOFTID test article in the 31-inch Mach 10 Air Tunnel, which is part of the Langley Aerothermodynamics Laboratory at the NASA Langley Research Center. The experiments are described in detail by Rodrigues et al. [21], and a brief summary is included here.

A picture of the test article mounted on the sting is shown in Fig. 8a, alongside a dimensioned drawing in Fig. 8b. Dimensions are provided in Table 2. The model features a 70-degree sphere cone as the representative heat shield with a concave back portion. One notable difference between the as-flown LOFTID geometry and the test article is the absence of toroidal rings on the aft side. The maximum diameter of the test article is 127 mm. The blade sting is mounted to one side to allow for measurements in the centerline of the sphere-cone, without direct interference. Nevertheless, an offset sting will still have an effect on a wake flow by damping the large-scale fluctuations, as shown by Stack et al. [26]. The origin for the coordinate system used in this paper is located at the nose of the vehicle. The relative orientation of the x, y, and z axes are shown in Fig. 2. The x direction is aligned with the centerline of the heat shield, such that $y = 0$, $z = 0$ is the centerline. The position $x/D = 0$ does not correspond to the start of the wake but rather the nose; this decision was made because the rear of the model is nonuniform, and there is no single x-location at which the separated wake begins. The separation occurs at the shoulder near $x/D = 0.176$ and the representative payload extends to $x/D = 0.293$.

The velocities in the wake were measured using planar laser-induced florescence (PLIF). The wake was seeded with nitric oxide (NO) from a series of 130 small holes with a 0.56 mm diameter, located on the aft side of the model. Velocity measurements were taken on a y-normal plane at $z = 0$. Both PLIF and Femtosecond laser electronic excitation tagging (FLEET) were used as two independent methods of measuring the velocity; the initial comparisons showed that the measurements generally agreed to within 10%. The PLIF measurements were obtained using a 10 Hz, pulsed, tunable UV laser, which was split into 75 laser beams near the test section using a diffractive optical element. For the test runs at a 0-degree angle of attack, approximately 67 laser lines were present in the wake. The laser wavelength

Table 2 Dimensions of the wind tunnel model, as shown in Fig. 8b

D	d_1	d_2	d_3	L_1	L_2	R_N	R_{C1}	R_{C2}
127 mm	25.7 mm	29.0 mm	35.1 mm	22.4 mm	14.8 mm	36.1 mm	2.3 mm	4.4 mm

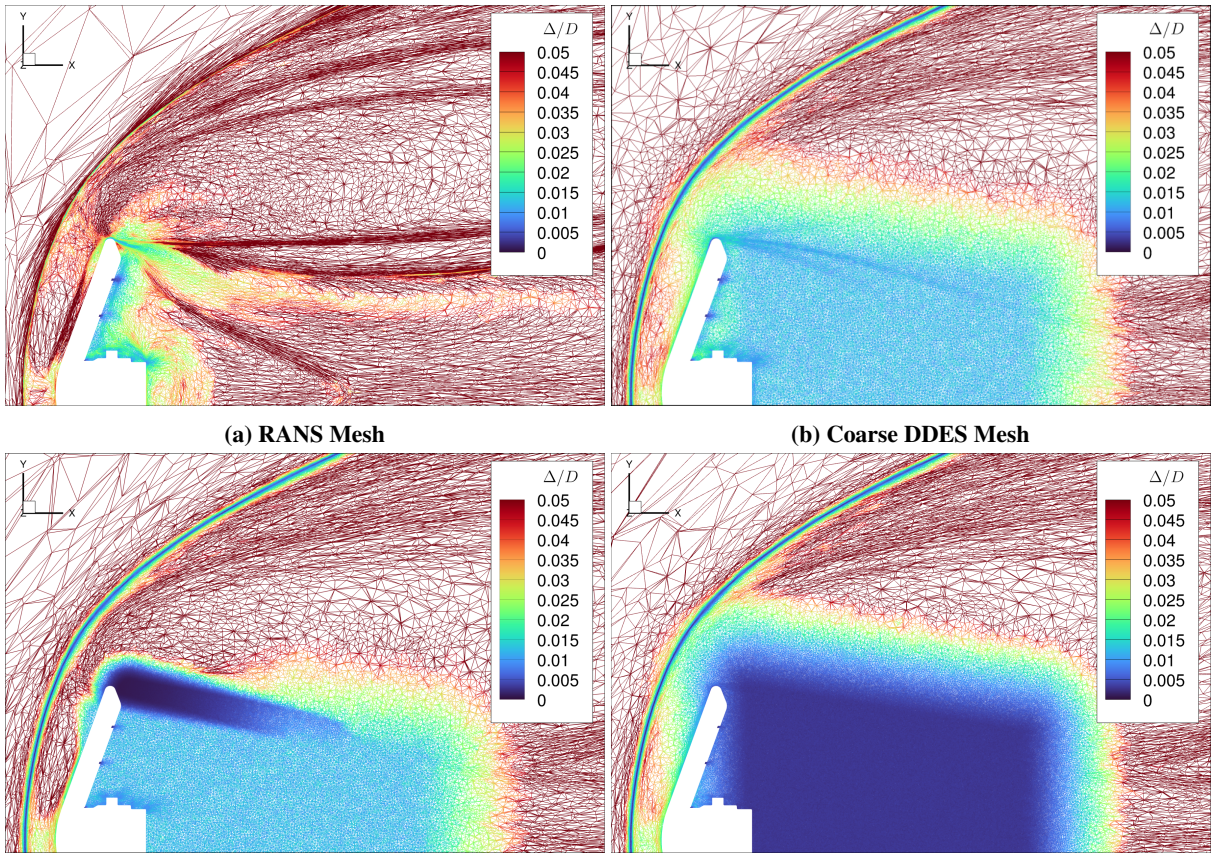

(a) RANS Mesh **(b) Coarse DDES Mesh**

(c) Coarse DDES Mesh with Shoulder Refinement **(d) Fine DDES Mesh**

Fig. 7 Meshes examined in the present work. The conditions match the $Re_D = 8.9 \times 10^5$case. The mesh is colored by the maximum edge length of a cell, nondimensionalized by the maximum diameter.

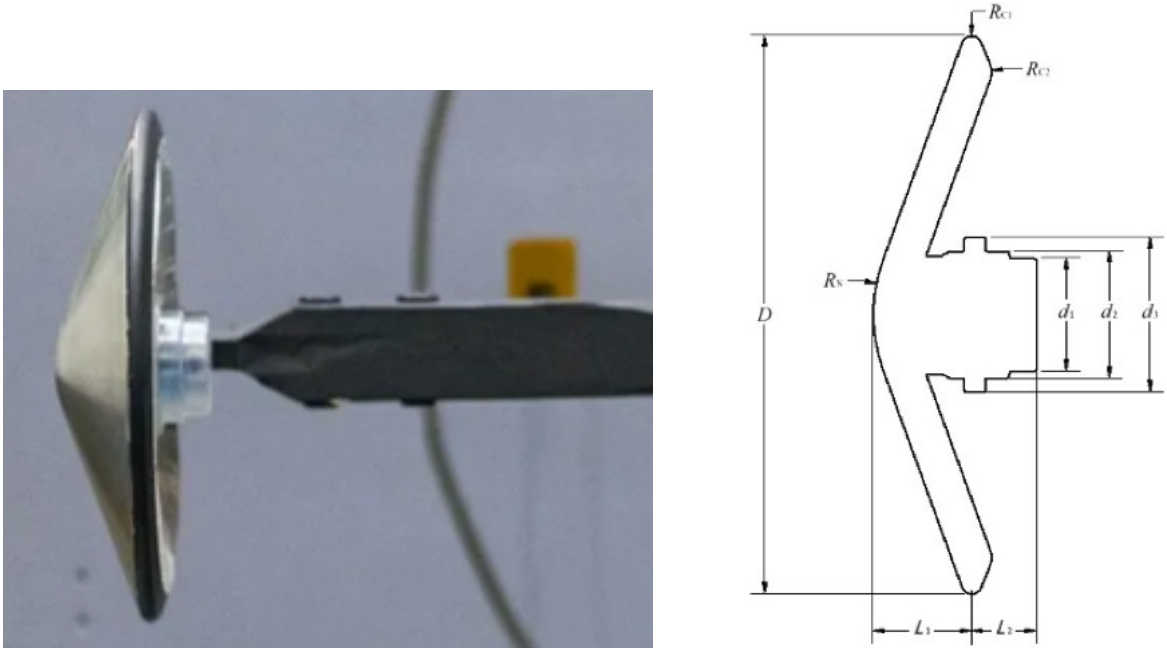

(a) Photo of the LOFTID model and sting **(b) Dimensioned drawing**

Fig. 8 The LOFTID model used for experiments

was tuned to excite nitric oxide (NO) molecules seeded into the wake through the holes in the aft section. The UV fluorescence was imaged using an intensified camera. By recording two successive images approximately 500 ns apart, the velocity can be determined based on the displacement of the fluorescence induced by the laser lines and the known time interval. Example snapshots of the fluorescence intensity are shown in Fig. 4. The parallel lines generated by the laser extended to about 120 mm, or approximately one diameter, downstream of the vehicle. About 120 single-shot images were used to calculate the time-averaged and RMS velocity.

Rodrigues et al. [21] reported the measurement error based on several experimental sources of error, including the uncertainties in the measured displacement of the laser lines, timing, and magnification. For comparison with CFD in the present work, the reported measurement uncertainty was combined with a heuristic uncertainty based on the observed asymmetry in the velocity measurements. This additional uncertainty was constructed such that both the reported mean velocity and the velocity mirrored across the $y = 0$ plane both lie within the uncertainty bands. The spatially-varying error bounds were defined as a function of the transverse direction y as follows:

$$u_{low}(x, y) = 1/2(\langle u(x, y)\rangle + \langle u(x, -y)\rangle) - \sqrt{\upsilon_m^2(x, y) + \upsilon_a^2(x, y)} \tag{1}$$

$$u_{high}(x, y) = 1/2(\langle u(x, y)\rangle + \langle u(x, -y)\rangle) + \sqrt{\upsilon_m^2(x, y) + \upsilon_a^2(x, y)} \tag{2}$$

where u_{low} and u_{high} are the estimated error bounds on the mean axial velocity, $\bar{u}(r)$ is the measured velocity at the position (x, y), υ_m is the reported measurement error, and υ_a is defined as:

$$\upsilon_a \equiv 1/2(\langle u(x, y)\rangle - \langle u(x, -y)\rangle) \tag{3}$$

or one-half the difference between the velocity measurement and the mirrored velocity measurement. This additional uncertainty has little effect near the centerline but greatly increases the uncertainty at the wake edge, where lower nitric oxide seed gas leads to a lower signal-to-noise ratio.

V. Results

Comparisons between CFD and the experimental data are presented in the following sections: The relative performance of different turbulence models is presented in Section V.A. Next the sensitivity to Reynolds number is

explored, both for the experimental data and the CFD solutions, in Section V.B. The sensitivity of the DDES results to mesh resolution are explored in Section V.C. Finally, a brief comparison is given between the results using FUN3D and HyperSolve to establish confidence in the repeatability of the present results. V.D.

A. Comparison of RANS and DDES Approaches

Previous research on supersonic wakes consistently shows that steady RANS models predict too strong a reverse velocity too close to the surface [15]. DDES is expected to perform much better at predicting the mean velocity, albeit with its own difficulties in predicting turbulence at the start of the shear layer [55–57]. This section compares wakeflow predictions between DDES and two steady RANS models: SA-neg and SST-Vm. Results for several other steady RANS models are shown in the Appendix.

Contour plots of the mean axial velocity at the lower and higher Reynolds numbers are shown in Fig. 9 and 10, respectively. These contour plots show the predictions of SST-Vm and DDES, compared with the experimental data. In these plots, the zero velocity contour line is specifically marked to demonstrate the extent of the separated region. As described in Section IV, the origin ($x = 0$) is centered on the nose rather than the separation point; the representative payload extends to $x/D = 0.293$, so the beginning of the contour plot at $x/D = 0.3$ is just behind the payload.

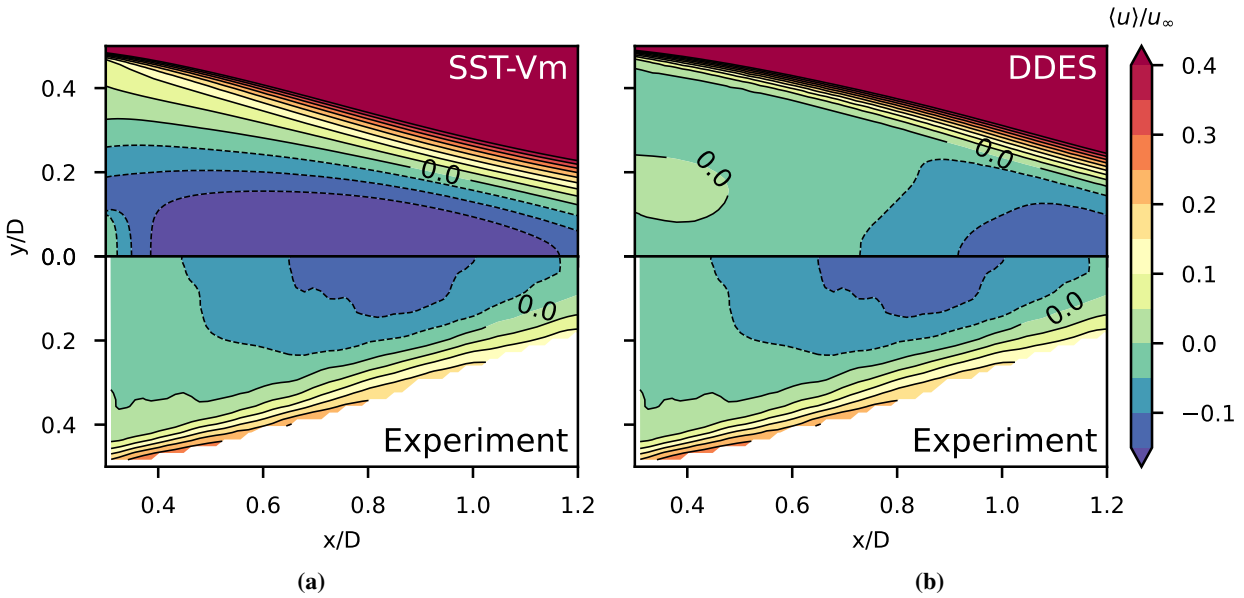

Fig. 9 Comparison of the CFD and experimental mean velocity fields at the lowest Reynolds number, $Re_D = 2.5 \times 10^5$. The zero-velocity contour line is labeled.

To better illustrate both the experimental uncertainty and the range of performances across several RANS models, velocity profiles are shown both along the centerline in Fig. 11 and along the transverse direction y at several x-locations in Figs 12 and 13. These plots include the experimental uncertainty as shaded regions in the plots. The transverse profiles at $x/D = 0.4$ and $x/D = 1.142$ are near the edges of the visualization window ($x/D = 0.4$ is about $0.1D$ downstream from the rear of the payload). The location $x/D = 0.85$ is close to the strongest reverse velocity measured in the experiments.

The steady RANS models, i.e., SA-neg, and SST-Vm, overestimate the magnitude of the maximum reverse velocity. The location of the local extrema in velocity is also too close to the test article; the experiments place the local minima somewhere in the range $0.8 < x/D < 0.95$ for both Reynolds numbers, while the RANS models place the local minima at $0.45 < x/D < 0.8$. The shear layer thickness is overpredicted, meaning that the gradient occurs over too wide a range of y/D. While the experimental data shows a flat region of near-zero velocity immediately behind the test article, e.g., at $x/D = 0.4$, the RANS has no such near-constant regions. Of the steady RANS models, the length of the recirculation region is best predicted by SST-Vm. The better performance of SST-Vm is consistent with previous studies on supersonic wakes [8, 58]. The failures of the SA-neg model are not surprising; the original SA-neg model was originally calibrated for 2D flows and no attempt was made to match axisymmetric flows [40]. Later additions, such

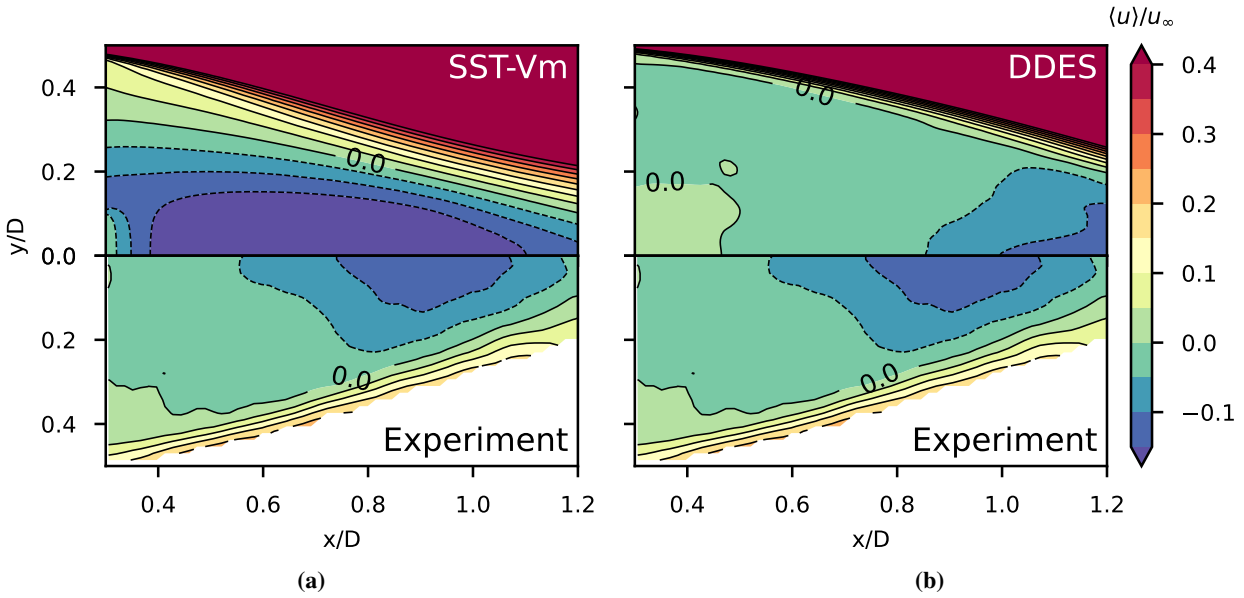

(a) (b)

Fig. 10 Comparison of the CFD and experimental mean velocity fields at the highest Reynolds number, $Re_D = 8.9 \times 10^5$. The zero-velocity contour line is labeled.

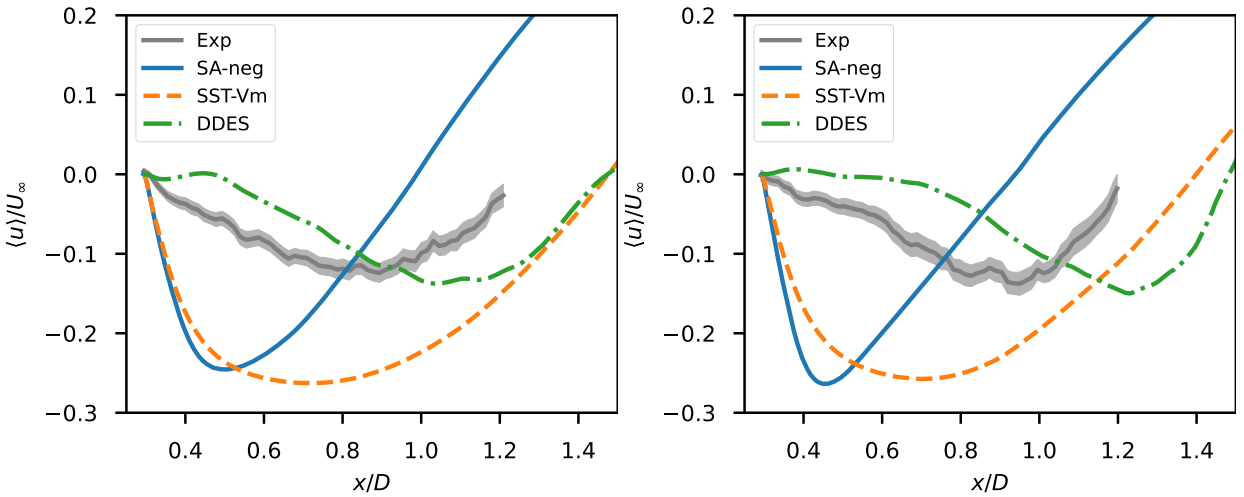

(a) $Re_D = 2.5 \times 10^5$ (b) $Re_D = 8.9 \times 10^5$

Fig. 11 The axial velocity along the centerline of the model, predicted using various turbulence models, for (a) the lower Reynolds number and (b) the higher Reynolds number cases.

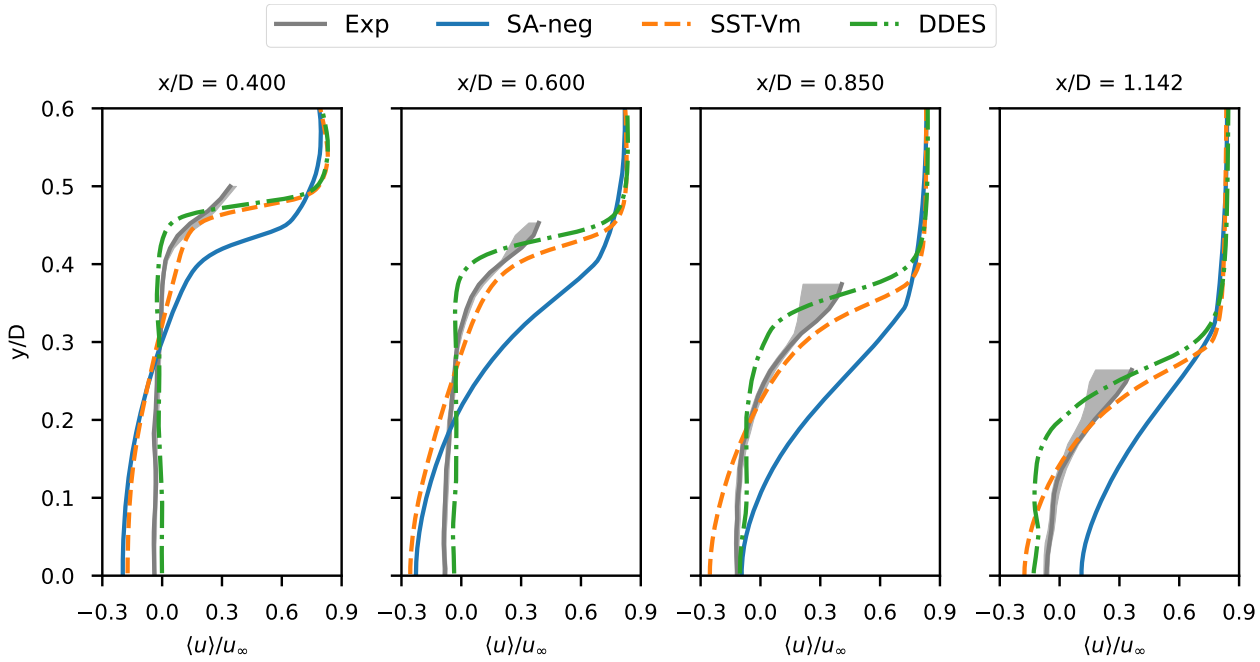

Fig. 12 Radial profiles at the lowest Reynolds number, $Re_D = 2.5 \times 10^5$

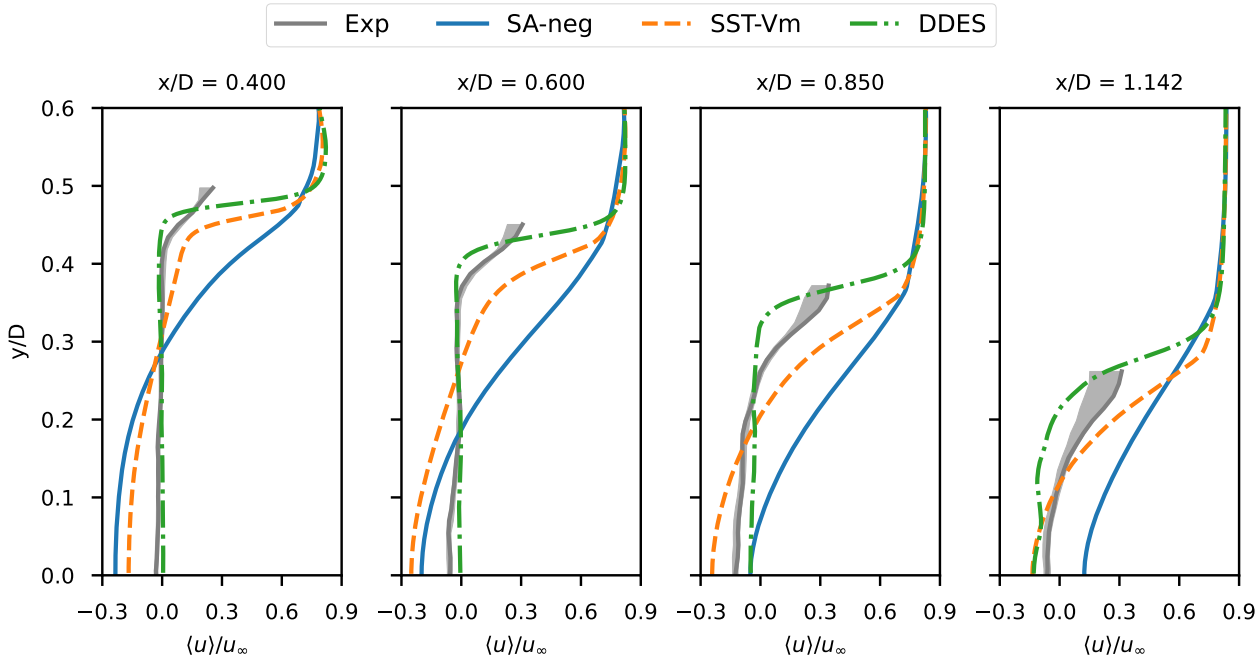

Fig. 13 Radial profiles at the highest Reynolds number, $Re_D = 8.9 \times 10^5$

as the Rotation-Curvature correction, do not completely address the model limitations.

DDES better captures the magnitude of the peak reverse velocity, predicting it to within $\pm 0.05 U\infty$. DDES also predicts a similar near-zero velocity region immediately behind the test article, as seen in Fig. 12 and 13. However, the detached shear layer is much too thin and there is a noticeable elongation of the separated wake. The maximum reverse velocity occurs too far downstream, as well as the zero-velocity wake closure. This shift was also noticed in a previous study on a Mach 6 axisymmetric wake [58].

B. Reynolds Number Trend

One important part of CFD validation is ensuring that the correct physical trends are observed as the Reynolds number is varied. Practical applications will cover a wide range of Reynolds numbers, so for CFD to be predictive at flight conditions it capture these Reynolds number trends. The PLIF data provides useful insight into how a hypersonic wake changes as the Reynolds number increases. The experimental campaign only spanned a small range of Reynolds numbers, from $Re_D = 2.51 \times 10^5$ on the low end and $Re_D = 8.93 \times 10^5$ at the high end. A more extensive testing campaign might reveal more about the changes in this flow between fully-laminar and fully-turbulent regimes. The measured velocity profiles both near the test article (e.g., $x/D \approx 0.4$) and further downstream (e.g. $x/D > 1$) are very similar across all Reynolds numbers. Nevertheless, there are several subtle trends seen in the experimental data as the Reynolds number increases. These trends can be seen in profiles of the time-averaged axial velocity, shown in Fig. 14 and 15. The differences are most pronounced near $x/D = 0.6$. Here, the lowest Reynolds number case has the strongest reverse velocity along the centerline. Additionally, the wake region where $\langle u \rangle < 0$ grows larger as the Reynolds number increases. For any radial position, the velocity gradients are largest at the lowest Reynolds number. Qualitatively, the higher Reynolds number cases demonstrate a distinct inflection point between the centerline and the wake edge. This waviness may be the imprint of the geometry of the backshell; as can be seen in Fig. 8a, the test article has a cylindrical payload that protrudes into the wake. At all three Reynolds numbers, the peak reverse velocity has a similar magnitude and location $x/D \approx 0.85$, with a slight shift downstream with increasing Reynolds number. A wider range of Reynolds numbers may be necessary to clearly demonstrate the Reynolds-number dependence of the peak reverse velocity.

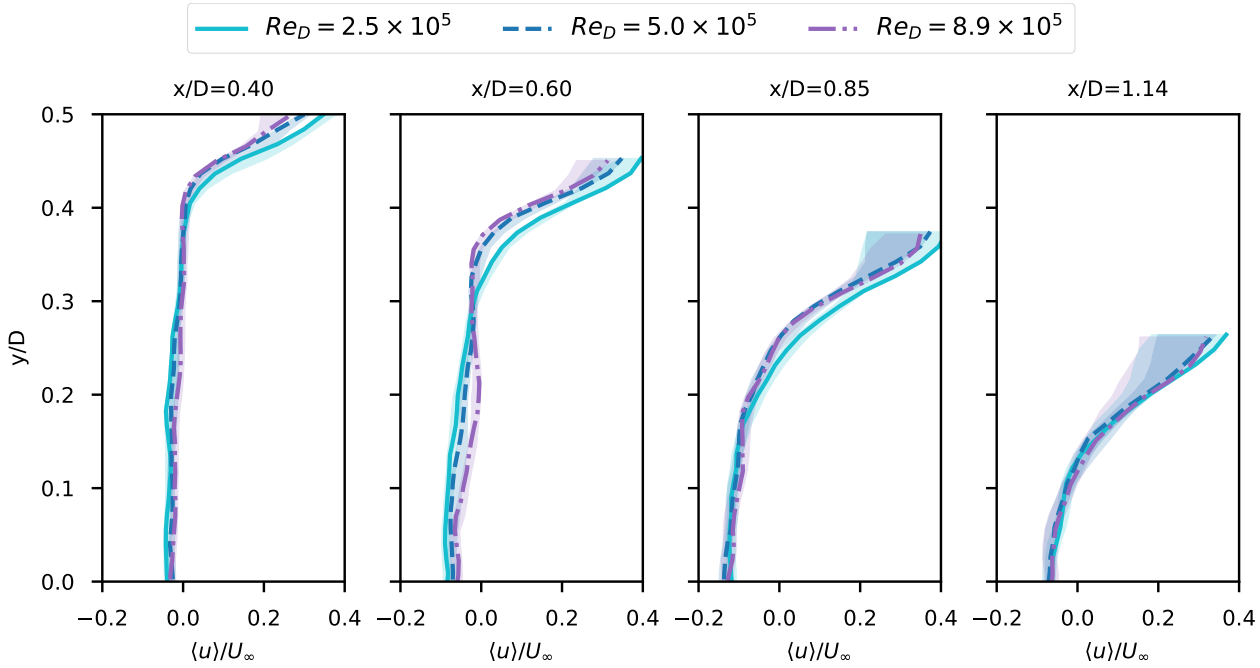

Fig. 14 Radial profiles showing only the experimental measurements at different Reynolds numbers. The shaded regions represent the uncertainty in the experimental data.

As depicted in Fig. 16, the DDES results display the same qualitative trends with Reynolds number. The wake region where $\langle u \rangle < 0$ grows larger, and the reverse velocity is strongest at the lowest Reynolds number. The detached shear layer decreases in thickness as the Reynolds number increases. These findings support the conclusion that the

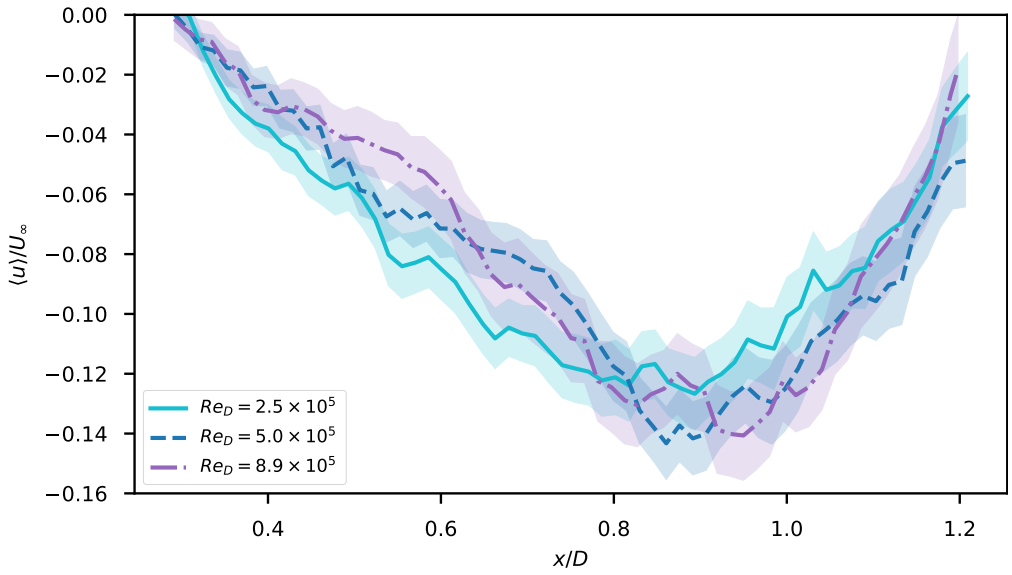

Fig. 15 Centerline profile showing only the experimental measurements at different Reynolds number. The shaded regions represent the uncertainty in the experimental data.

DDES is capturing the qualitative nature of the physics properly, even if there is an overprediction of the size of the recirculation region. They also demonstrate that the impact of uncertainty in the freestream conditions is relatively small. Small discrepancies in Reynolds number would not change the solution enough to explain some of the differences between CFD and experiment.

C. Mesh-Sensitivity of DDES

A mesh refinement study with four different meshes demonstrates the impact of mesh resolution on the DDES solution. DDES is an inappropriate model when the mesh is too coarse to resolve the turbulent fluctuations in separated regions. The coarsest wake resolution was $\Delta/D \approx 1\%$, which is similar to the resolution of the finest mesh used by Sinha and Candler [19]. Two finer meshes were used, with spacing of 0.5% and 0.25% of the diameter. Additionally, the effect of refinement near separation was examined by applying a fine mesh spacing in a small region at the shoulder. This region is shown in Fig. 7c. The timesteps were smaller on the finer meshes to maintain a wake CFL of approximately $\Delta t u/\Delta x \approx 1$, where u is the local velocity. More total timesteps were used for the finer meshes, to average over the same period of $240D/U_\infty$. Due to the transitional character of this flow, the shear layer near the separation point has relatively small length scales. The initial shear layer and the refinement around the separation point are shown in Fig. 18 for the coarse DDES mesh with shoulder refinement. The mesh with shoulder refinement has cells that are about eight times smaller in this region.

The mean axial velocity is shown in Figures 19 and 20. The region closest to the test article appears to be most sensitive to the mesh resolution and is closer to the experimental data with finer grids. However, the location of the minimum velocity is similar for all meshes. The shear layer is too thin on all meshes and does not thicken with increasing resolution. These trends match those observed by Sinha and Candler [19], who observed a thinner shear layer and

Table 3 Description of the meshes used for the DDES solutions

Grid	Wake Δ/D	Shoulder Δ/D	Total Nodes	$\Delta t u_\infty/D$
Coarse	1%	1%	12.1 million	4.0×10^{-2}
Medium	0.5%	0.5%	44.5 million	2.0×10^{-2}
Fine	0.25%	0.25%	91.9 million	9.8×10^{-3}
Shoulder Refinement	1%	0.03%	106.1 million	4.0×10^{-2}

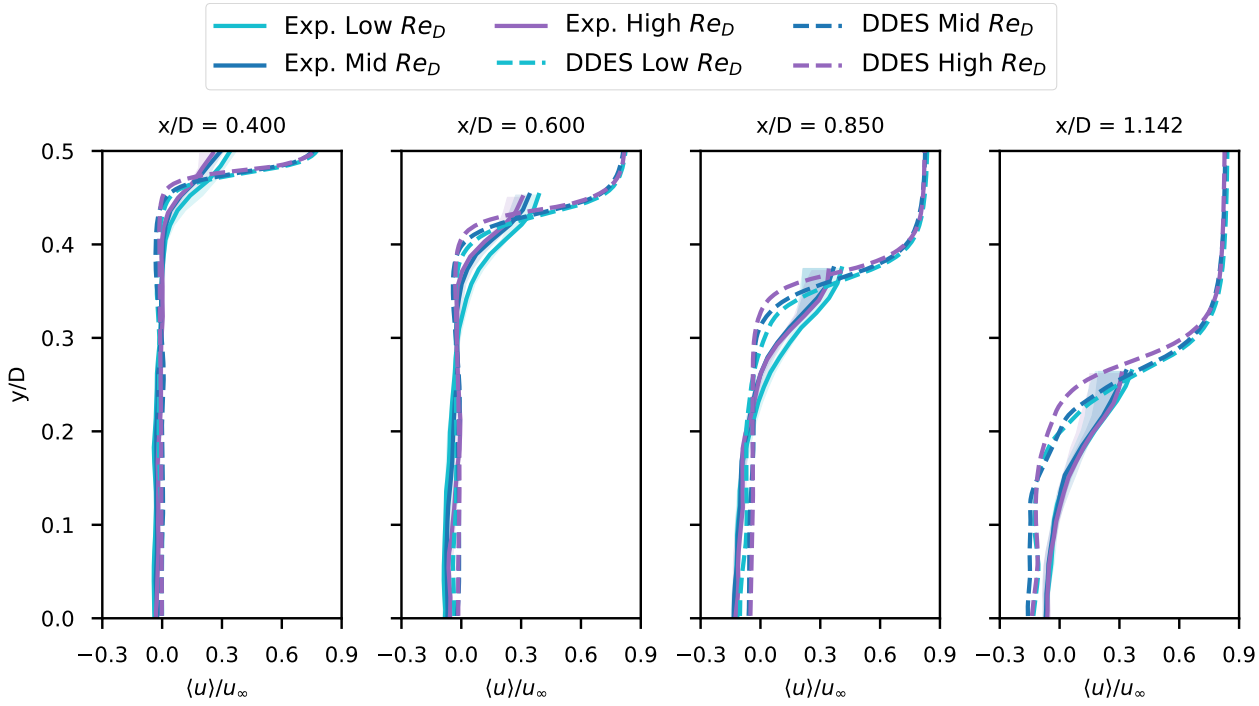

Fig. 16 Radial profiles showing the time-averaged axial velocity from the DDES at different Reynolds numbers.

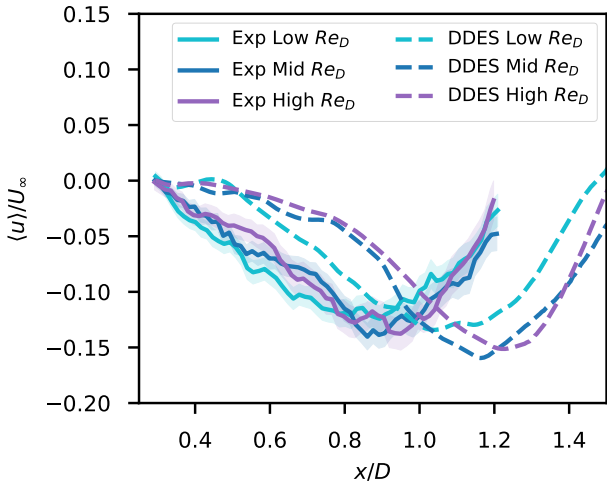

Fig. 17 Radial profiles of the time-averaged axial velocity from the DDES at different Reynolds numbers.

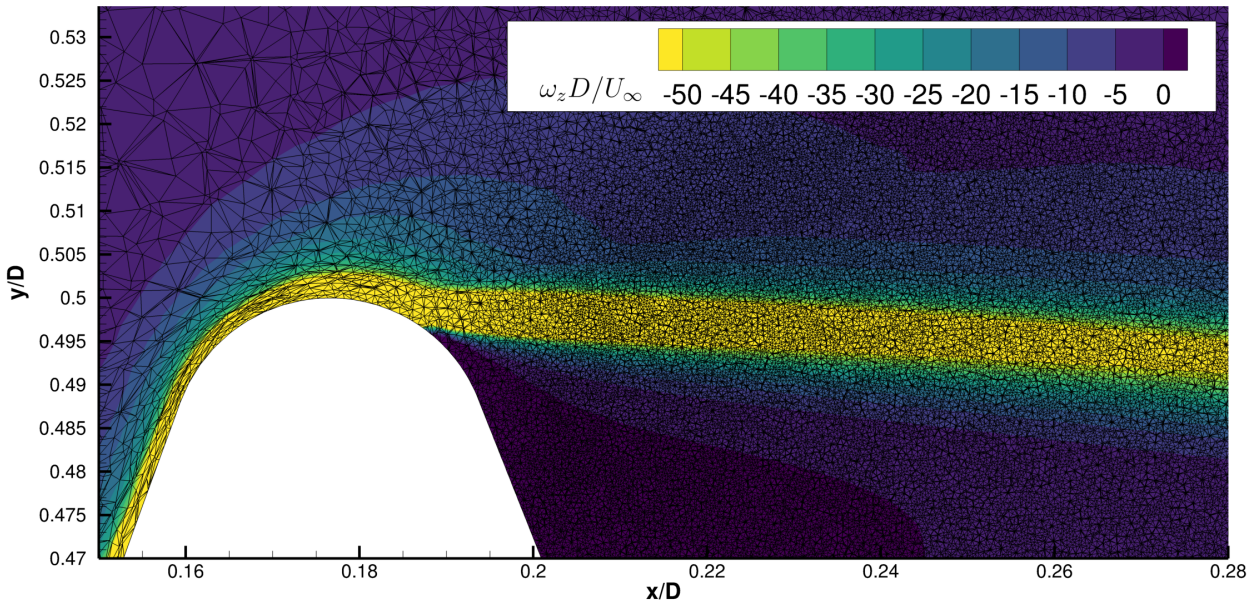

Fig. 18 A slice through the DDES mesh with refinement near the separation point. The contours show the component of vorticity that is normal to the slice.

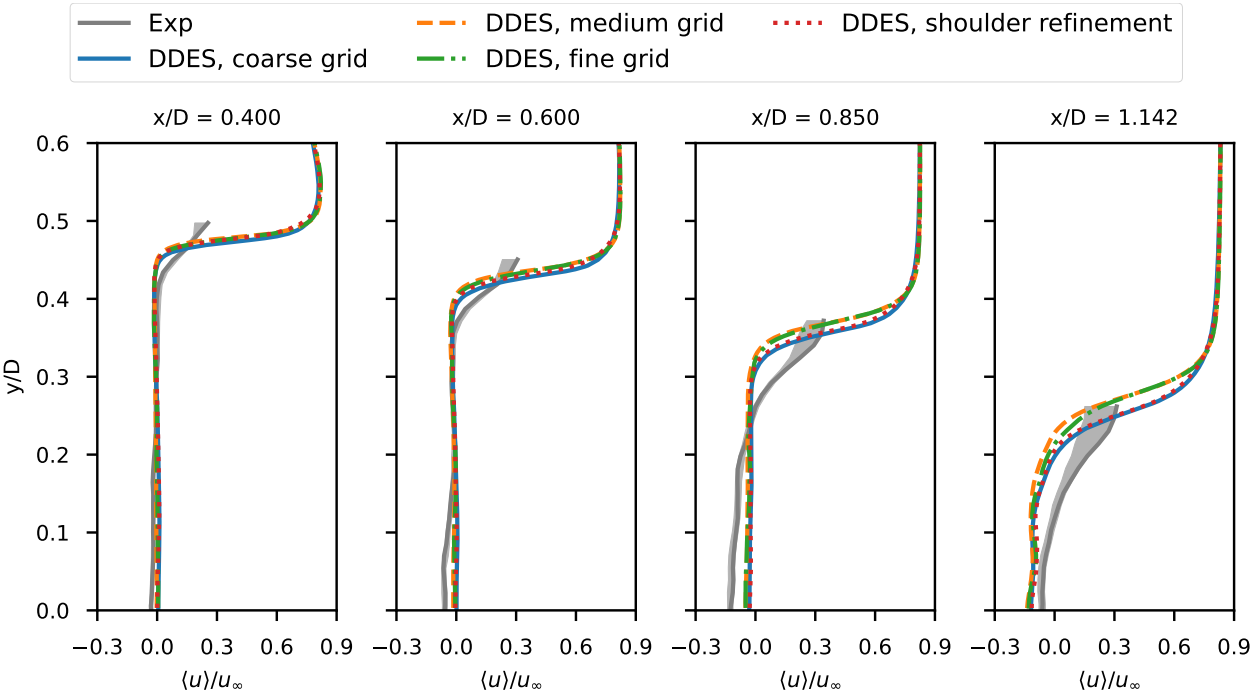

Fig. 19 Radial profiles of the axial velocity at the highest Reynolds number, $Re_D = 8.9 \times 10^5$, using DDES and a series of finer meshes.

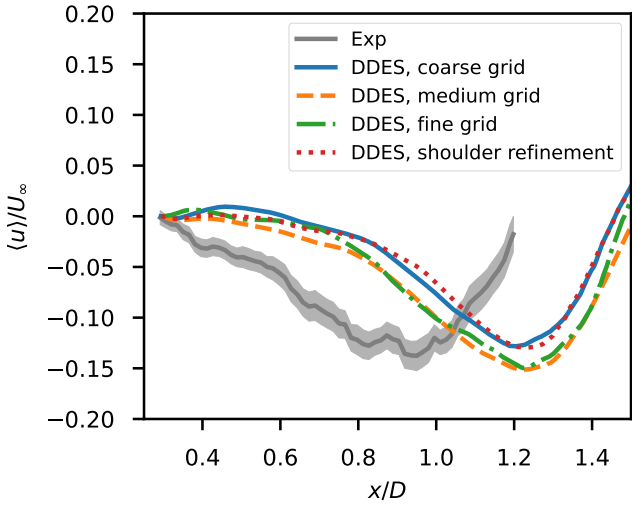

Fig. 20 Centerline profile of the axial velocity at the highest Reynolds number, $Re_D = 8.9 \times 10^5$, using DDES and a series of finer meshes.

larger separated wake on finer meshes. Additionally, localized refinement at the shoulder does not have a large impact on solution accuracy. This mesh sensitivity study demonstrates that for unstructured tetrahedral meshes and mesh resolutions between $\Delta/D = 1\%$ and $\Delta/D = 0.25\%$, a finer mesh does not remedy the modeling errors.

The instantaneous PLIF images from the experiments shown in Fig. 4 show a relatively thin, nearly laminar shear layer close to the separation point. While there are a range of fluctuations further downstream that suggest turbulent flow, the region near the base appears to be near-laminar even at the highest Reynolds number tested. Capturing this transitional flow seems to be challenging for scale-resolving simulations. To illustrate the vortical structures in the unsteady solution, the isosurfaces of the Q-criterion are shown in Figs. 21 and 22 for the coarse and fine meshes, respectively. The Q-criterion can highlight vortex-dominated portions of the flow as opposed to shear-dominated portions, and is calculated as:

$$Q = 1/2(\Omega_{ij}\Omega_{ij} - S_{ij}S_{ij}) \tag{4}$$

where S is the rate-of-strain tensor and Ω is the rate-of-rotation tensor for the instantaneous velocity field. Three distinct regions appear in the isosurfaces of the Q-criterion: (1) the strong vorticity immediately following separation, (2) the vortices in the subsonic core of the wake, and (3) the outer portion of the shear layer, seen in Fig. 22a but not Fig. 22b, that envelopes the wake and only breaks down slowly into chaotic fluctuations. There is substantial vorticity near the separation point, but the shear layer does not immediately break down into Kelvin-Helmholtz instabilities. Instead, the resolved vortices appear further downstream and are mostly contained inside the recirculation region. Very few resolved fluctuations appear on the supersonic side of the shear layer. The sting also suppresses the formulation of turbulent eddies on the negative z side of the wake; there is a noticeable difference in the number of eddies in the positive z and negative z directions.

In the wake region, the modeled eddy viscosity μ_t is negligible. This can be seen in Fig. 23a, where the eddy-viscosity ratio $\mu_t/\mu \ll 1$ for most of the wake. The small values of μ_t indicate that the RANS model is contributing very little to the flow physics in the wake. However, the resolved kinetic energy is also very small over much of the wake. This is plotted in Fig. 23b for the highest Reynolds number case. This plot shows the ratio of resolved kinetic energy to the freestream kinetic energy, $2k/U_\infty^2 = \langle u_i' u_i' \rangle / U_\infty^2$, where $u_i' = u_i - \langle u_i \rangle$. In the initial portion of the shear layer, only a small fraction of the total energy is due to unsteady fluctuations. Further research could investigate the resolution of the initial shear layer on even finer meshes. Structured mesh regions may also be required to capture the physics of laminar-to-turbulent transition at a reasonable mesh budget.

One open question is the impact of the numerical dissipation on the current results. On the finest grids, the cell size in the wake is comparable to or finer than similar studies of supersonic blunt-body wakes. However, the scale of the mesh is only one part of the resolving-power of a convective scheme; both the cell size and the numerical scheme determine what scale of turbulent fluctuations can be resolved. Inviscid fluxes can act as a numerical filter, dissipating out the finer-scales of turbulence. At a fixed cell size, low-dissipation numerical schemes can resolve a broader range

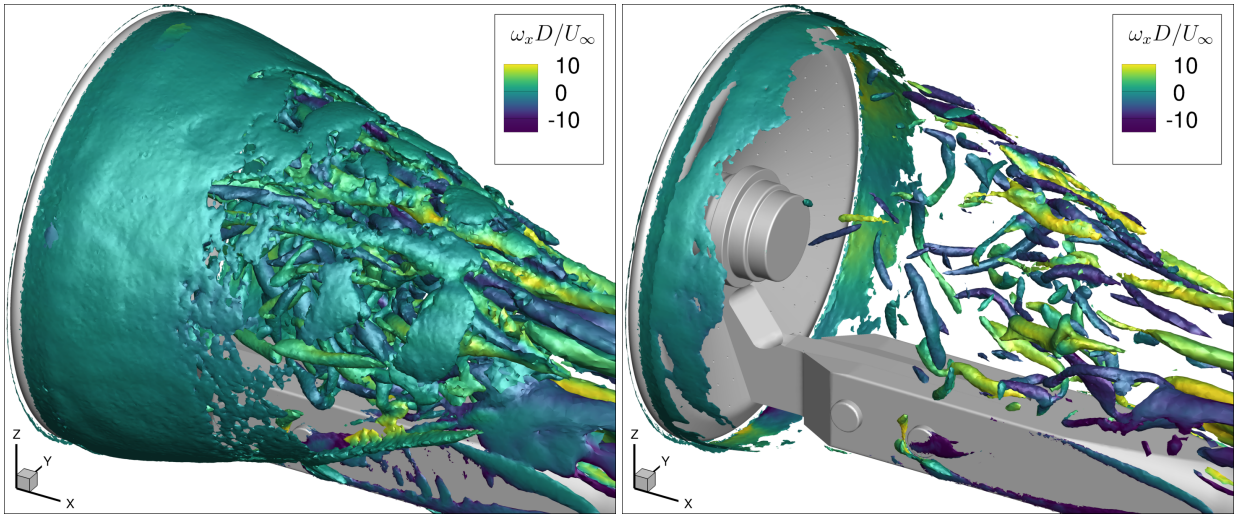

(a) $QD^2/U_\infty^2 = 2$ **(b)** $QD^2/U_\infty^2 = 10$

Fig. 21 Isosurfaces of the Q-criterion for the $Re_D = 8.9 \times 10^5$case using the coarsest DDES grid. The isosurfaces are colored by the vorticity in the axial direction.

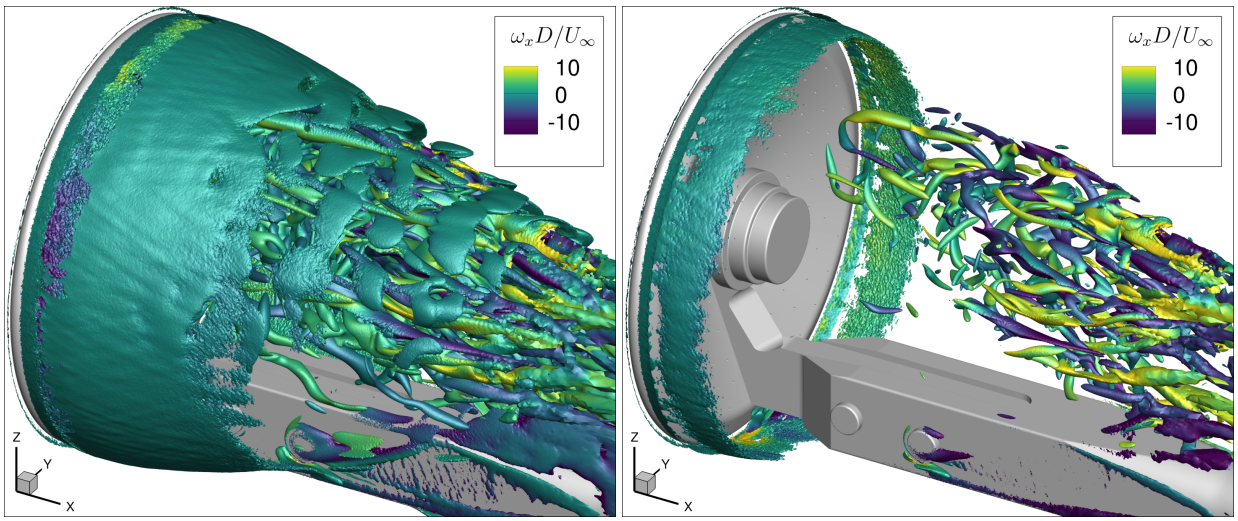

(a) $QD^2/U_\infty^2 = 2$ **(b)** $QD^2/U_\infty^2 = 10$

Fig. 22 Isosurfaces of the Q-criterion for the $Re_D = 8.9 \times 10^5$case using the fine DDES grid. The isosurfaces are colored by the vorticity in the axial direction.

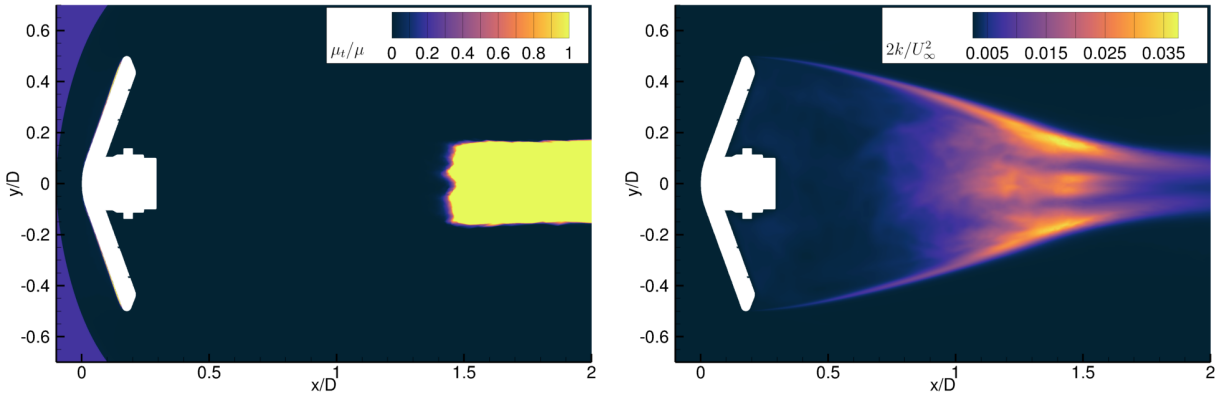

(a) Eddy-viscosity ratio **(b) Resolved turbulent kinetic energy**

Fig. 23 Plots of the (a) eddy viscosity ratio and (b) resolved turbulent kinetic energy in the flow along the $z = 0$ plane at $Re_D = 8.9 \times 10^5$.

of velocity fluctuations. Further research should examine the impact of low-dissipation schemes, such as economical higher-order schemes [59] and kinetic-energy and entropy-preserving schemes [60, 61]. Nevertheless, multiple studies on the wake of a supersonic cylindrical base flow [56, 57, 62] have found that improved numerics do not always produce a better prediction of supersonic separated wake flows. Their studies used low-dissipation numerical schemes and fine grids to better resolve the turbulent fluctuations at the start of the detached shear layer, resulting in a smaller recirculation region. However, this increased resolution also led to underpredictions of the velocity in the wake core, meaning that the reverse velocity was too large. These studies illustrate that numerical dissipation is only part of the overall error in CFD.

D. Comparison Across Solvers

The RANS cases were also used to examine how sensitive the solutions are to the differences in mesh adaptation and the numerics between solvers. As discussed in Section III, two compressible finite-volume codes were compared: FUN3D and HyperSolve. Both codes use the *refine* library to perform the meshing, but the discretizations are different and the discretization errors drive the mesh adaption. Because mesh adaptation was conducted independently in each flow solver, there was no expectation that the two codes would yield the exact same solution. Only the highest Reynolds number was examined and only the SA-neg and DDES models were compared. A plot of the transverse velocity profiles using the two solvers is shown in Fig. 24. There are only small differences between the solvers. For the SA-neg results, FUN3D predicts a more diffuse edge to the wake, which may be due to differences in the convective scheme. FUN3D uses a first-order convection scheme for the turbulence equations while HyperSolve allows for second-order convection, which can better resolve the edge of the turbulent wake. For the DDES results, the differences are also small and can be attributed to statistical uncertainty in the time-averaging. These comparisons provide confidence that the current results are not specific to the code or the computational mesh.

VI. Conclusions

Laser-based velocimetry data from an experimental campaign was compared with CFD predictions for a Mach 10 wake behind a simplified HIAD geometry. Neither RANS nor DDES accurately predicted the correct shear layer thickness nor the size of the separated wake region. As demonstrated in previous studies, the RANS models greatly overpredicted the magnitude of the reverse velocity in the separated wake. DDES performed much better in predicting the qualitative nature of the wake; the reverse velocity was predicted to within ±5% of the freestream velocity. DDES also demonstrates the correct trends with increasing Reynolds number. However, the DDES simulations overpredicted the length of the separation bubble. This failure is due to an underprediction of the shear layer thickness, which is likely due to a deficit in the resolved turbulent kinetic energy in the shear layer. These model failures were present not only on coarse grids, but on grids with a wake resolution of approximately 0.25% of the model diameter. Comparisons between the two CFD solvers, HyperSolve and FUN3D, showed good agreement for both steady and unsteady approaches. Future research should focus on improved models for HRLES and wall-modeled LES, with a focus on hypersonic flows and

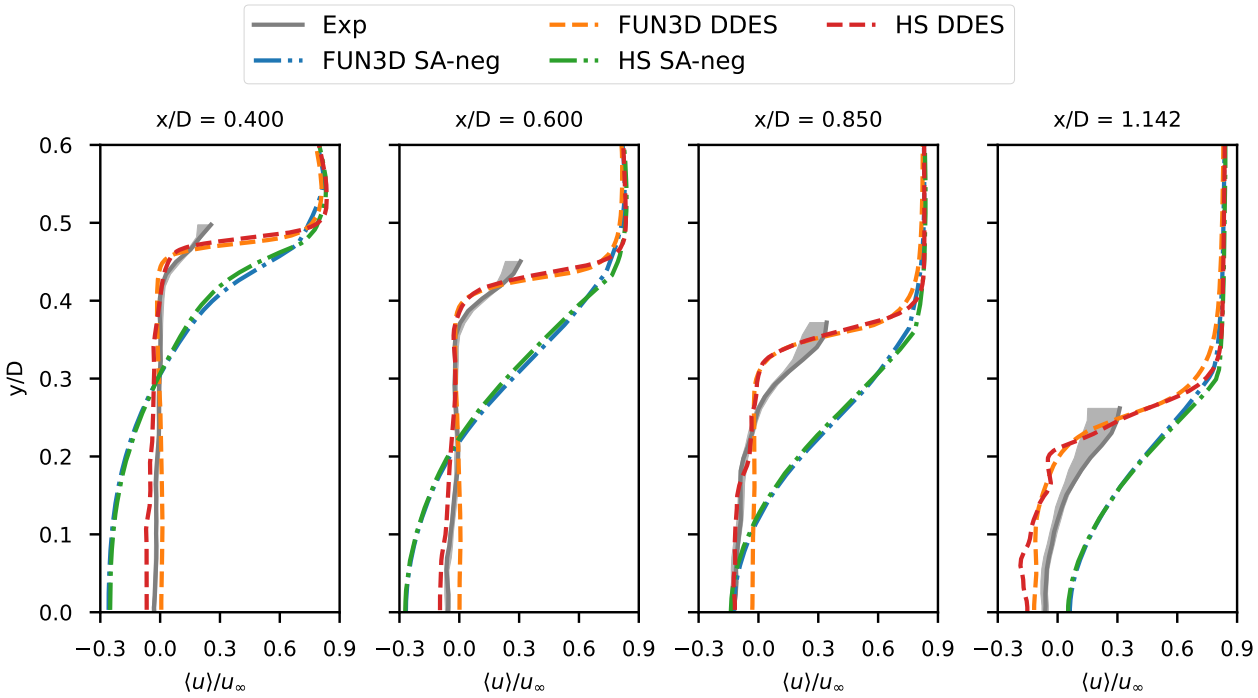

Fig. 24 Comparison of the transverse velocity profiles predicted by HyperSolve and FUN3D

lower Reynolds numbers. One promising idea is to introduce turbulent fluctuations through stochastic forcing, as in the Active Model Split [63] or the active approach of Mehta et al. [64]. Exciting the correct level of turbulent fluctuations could improve predictions of the detached shear layer and better match the physics of this complex wake flow.

This comparison between CFD and experiment illustrates the value of non-intrusive flow measurements such as PLIF for flight projects. These data can not only distinguish which models are grossly in error, but they can also be used to guide modeling towards the correct physics. Information on the shear layer provides insight into the relative over- or underprediction of the turbulent stresses. This information is harder to obtain from surface pressures, which is connected more loosely with the computational mesh or the turbulence model. Future work is planned to compare the RMS velocity data from the PLIF with CFD, as well as conduct additional experiments to measure multiple velocity components using PLIF.

Acknowledgments

The authors would like to thank the Entry Systems Modeling Project within the NASA Game Changing Development Program, Space Technology Mission Directorate for their funding and support of this research. The authors thank Dr. Paul Danehy and Olivia Tyrrell for their efforts involving the NO-PLIF test data acquisition. Kyle Thompson, Bill Wood, Bil Kleb, and Brian Hollis have provided frequent feedback and fruitful discussions which shaped this paper. Credit is also owed to all those involved in the wake flow task for Entry Systems Modeling, including J.B. Scoggins, Dirk Ekelschot, Aaron Erb, and Thomas West. Computing resources supporting this work were provided through the NASA K-Cluster at NASA Langley Research Center.

Appendix

A more complete comparison of steady RANS models was conducted at the higher Reynolds number ($Re_D = 8.9 \times 10^5$). This comparison includes a version of the Spalart-Allmaras model with a compressibility correction developed by Catris and Aupoix [65]. The compressibility correction was designed to provide the correct log-law behavior in attached boundary layers. Note that the version of SA-Catris implemented in FUN3D and HyperSolve is what the Turbulence Modeling Resource calls "SA-noft2-CatrisCons." The trip term is not implemented, and the conservative form of the convective operator is used. The conservative form matches the underlying physics and was

shown by Waligura et al. [66] to give good predictions for a shock boundary-layer interaction.

The transverse profiles are shown in Fig. 25. The results with SA-neg and SA-neg-RC differ, but the RC correction does not consistently improve agreement with experiment. The SA-Catris model may be slightly better near the shear layer, but it increases errors in the centerline velocity at $x/D \approx 0.6$. SST-Vm is consistently the closer to the experiments than any of the SA model variants examined. Near the test article (at $x/D = 0.4$ and $x/D = 0.6$), the DDES model gives better predictions than any of the steady RANS models despite its shortcomings.

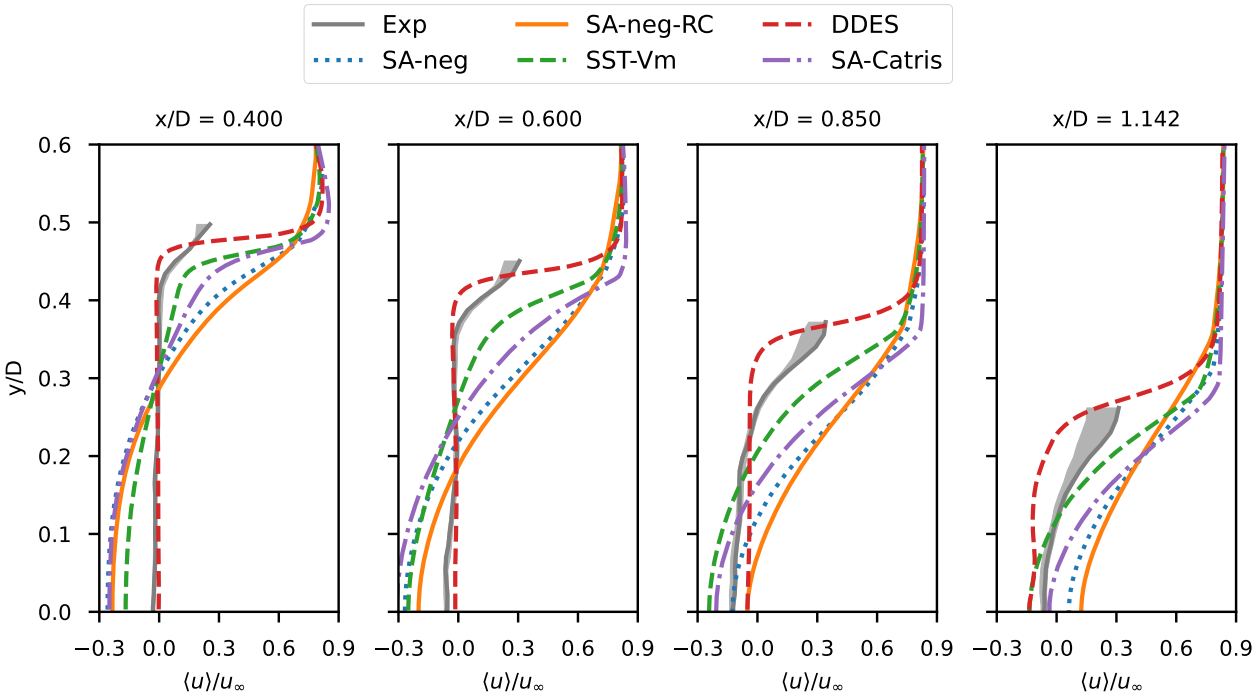

Fig. 25 A comparison of RANS and DDES turbulence models at the higher Reynolds number, $Re_D = 2.5 \times 10^5$

References

[1] Polsgrove, T., and Dwyer-Cianciolo, A. M., "Human Mars Entry, Descent and Landing Architecture Study Overview," *AIAA SPACE 2016*, American Institute of Aeronautics and Astronautics, Long Beach, California, 2016. https://doi.org/10.2514/6.2016-5494.

[2] Bose, D. M., Shidner, J., Winski, R., Zumwalt, C., Cheatwood, F. M., and Hughes, S. J., "The Hypersonic Inflatable Aerodynamic Decelerator (HIAD) Mission Applications Study," *AIAA Aerodynamic Decelerator Systems (ADS) Conference*, American Institute of Aeronautics and Astronautics, Daytona Beach, Florida, 2013. https://doi.org/10.2514/6.2013-1389.

[3] DiNonno, J., and Cheatwood, F. M., "Low-Earth Orbit Flight Test of an Inflatable Decelerator (LOFTID) Mission Overview, Science Return, and Future Applications of This Technology," *20th International Planetary Probe Workshop*, Marseille, France, 2023.

[4] Campbell, J. F., and Brown, C. A., "Experimental Wake Flow Properties of a Viking '75 Entry Vehicle," *Journal of Spacecraft and Rockets*, Vol. 11, No. 1, 1974, pp. 11–15. https://doi.org/10.2514/3.61997.

[5] Wilcox, D. C., *Turbulence Modeling for CFD*, 3rd ed., DCW Industries, La Cãnada, California, 2006.

[6] Wilcox, D., "Progress in Hypersonic Turbulence Modeling," *22nd Fluid Dynamics, Plasma Dynamics and Lasers Conference*, American Institute of Aeronautics and Astronautics, Honolulu, HI, U.S.A., 1991. https://doi.org/10.2514/6.1991-1785.

[7] Rumsey, C. L., "Compressibility Considerations for K-Omega Turbulence Models in Hypersonic Boundary Layer Applications," NASA TM 2009-215705, NASA Langley Research Center, Hampton, VA, Apr. 2009.

[8] Pederson, C., and Schoenenberger, M., "Exploring the Accuracy of RANS Simulations for Mars Entry Vehicles," *AIAA Aviation 2023 Forum*, American Institute of Aeronautics and Astronautics, San Diego, CA, 2023. https://doi.org/10.2514/6.2023-3695.

[9] Spalart, P., "Trends in Turbulence Treatments," *Fluids 2000 Conference and Exhibit*, AIAA, Denver, CO, 2000. https://doi.org/10.2514/6.2000-2306.

[10] Spalart, P. R., Jou, W., Strelets, M., and Allmaras, S. R., "Comments on the Feasibility of LES for Wings, and on a Hybrid RANS/LES Approach," *Advances in DNS/LES, 1st AFOSR Int Conf*, Columbus, OH, 1997.

[11] Spalart, P. R., "Detached-Eddy Simulation," *Annual Review of Fluid Mechanics*, Vol. 41, 2009, pp. 181–202. https://doi.org/10.1146/annurev.fluid.010908.165130.

[12] Spalart, P. R., Deck, S., Shur, M. L., Squires, K. D., Strelets, M. Kh., and Travin, A., "A New Version of Detached-eddy Simulation, Resistant to Ambiguous Grid Densities," *Theoretical and Computational Fluid Dynamics*, Vol. 20, No. 3, 2006, pp. 181–195. https://doi.org/10.1007/s00162-006-0015-0.

[13] Fröhlich, J., and von Terzi, D., "Hybrid LES/RANS Methods for the Simulation of Turbulent Flows," *Progress in Aerospace Sciences*, Vol. 44, No. 5, 2008, pp. 349–377. https://doi.org/10.1016/j.paerosci.2008.05.001.

[14] Heinz, S., "A Review of Hybrid RANS-LES Methods for Turbulent Flows: Concepts and Applications," *Progress in Aerospace Sciences*, Vol. 114, 2020, p. 100597. https://doi.org/10.1016/j.paerosci.2019.100597.

[15] Forsythe, J. R., Squires, K. D., Wurtzler, K. E., and Spalart, P. R., "Detached-Eddy Simulation of the F-15E at High Alpha," *Journal of Aircraft*, Vol. 41, No. 2, 2004, pp. 193–200. https://doi.org/10.2514/1.2111.

[16] Barnhardt, M., Candler, G., and MacLean, M., "CFD Analysis of CUBRC Base Flow Experiments," *48th AIAA Aerospace Sciences Meeting Including the New Horizons Forum and Aerospace Exposition*, American Institute of Aeronautics and Astronautics, Orlando, Florida, 2010. https://doi.org/10.2514/6.2010-1250.

[17] Barnhardt, M., and Candler, G. V., "Detached-Eddy Simulation of the Reentry-F Flight Experiment," *Journal of Spacecraft and Rockets*, Vol. 49, No. 4, 2012, pp. 691–699. https://doi.org/10.2514/1.A32128.

[18] Brock, J. M., Subbareddy, P. K., and Candler, G. V., "Detached-Eddy Simulations of Hypersonic Capsule Wake Flow," *AIAA Journal*, Vol. 53, No. 1, 2015, pp. 70–80. https://doi.org/10.2514/1.J052771.

[19] Sinha, K., and Candler, G., "Grid Sensitivity of Detached Eddy Simulation of a Mach 16 Re-Entry Configuration," *45th AIAA Aerospace Sciences Meeting and Exhibit*, American Institute of Aeronautics and Astronautics, Reno, Nevada, 2007. https://doi.org/10.2514/6.2007-1115.

[20] Schwing, A. M., and Candler, G. V., "Detached-Eddy Simulation of Capsule Wake Flows and Comparison to Wind-Tunnel Test Data," *Journal of Spacecraft and Rockets*, Vol. 52, No. 2, 2015, pp. 439–449. https://doi.org/10.2514/1.A32834.

[21] Rodrigues, N. S., Tyrrell, O. K., Rieken, E., Hollis, B. R., and Danehy, P. M., "FLEET and PLIF Velocimetry within a Mach 10 Hypersonic Air Flow," *AIAA SciTech 2024 Forum*, American Institute of Aeronautics and Astronautics, Orlando, FL, 2024. https://doi.org/10.2514/6.2024-2323.

[22] Rodrigues, N. S., Tyrrell, O. K., Danehy, P. M., Rieken, E. F., Hollis, B. R., Ripley, W. H., Crider, J. B., Robbins, A. W., Reynolds, T., and Wright, S. A., "Application of PLIF to Investigate the Hypersonic Wake of a LOFTID-Relevant Model at Mach 10," NASA TM 20240000817, NASA Langley Research Center, Hampton, VA, Apr. 2024.

[23] Herrin, J. L., and Dutton, J. C., "Supersonic Base Flow Experiments in the near Wake of a Cylindrical Afterbody," *AIAA Journal*, Vol. 32, No. 1, 1994, pp. 77–83. https://doi.org/10.2514/3.11953.

[24] Sandberg, R. D., and Fasel, H. F., "Direct Numerical Simulations of Transitional Supersonic Base Flows," *AIAA Journal*, Vol. 44, No. 4, 2006, pp. 848–858. https://doi.org/10.2514/1.18177.

[25] Kirchner, B. M., Favale, J. V., Elliott, G. S., and Dutton, J. C., "Three-Component Turbulence Measurements and Analysis of a Supersonic, Axisymmetric Base Flow," *AIAA Journal*, Vol. 57, No. 6, 2019, pp. 2496–2512. https://doi.org/10.2514/1.J057859.

[26] Stack, C., Dechant, L., Robbins, B., Zhang, Y., and Casper, K., "Influence of Blunt-Body Base Protuberances on Near-Wake Unsteadiness." *ICCFD11*, Maui, Hawaii, 2022. https://doi.org/10.2172/2003980.

[27] Freund, J. B., Lele, S. K., and Moin, P., "Compressibility Effects in a Turbulent Annular Mixing Layer. Part 1. Turbulence and Growth Rate," *Journal of Fluid Mechanics*, Vol. 421, 2000, pp. 229–267. https://doi.org/10.1017/S0022112000001622.

[28] Hollis, B. R., "Real-Gas Flow Properties for NASA Langley Research Center Aerothermodynamic Facilities Complex Wind Tunnels," NASA CR 4755, NASA Langley Research Center, Hampton, VA, Sep. 1996.

[29] Hollis, B. R., and Collier, A. S., "Turbulent Aeroheating Testing of Mars Science Laboratory Entry Vehicle," *Journal of Spacecraft and Rockets*, Vol. 45, No. 3, 2008, pp. 417–427. https://doi.org/10.2514/1.31798.

[30] Anderson, W. K., Biedron, R. T., Carlson, J.-R., Derlaga, J. M., Druyor, C. T., Gnoffo, P. A., Hammond, D. P., Jacobson, K. E., Jones, W. T., Kleb, W., Lee-Rausch, E. M., Nastac, G., Nielsen, E. J., Park, M. A., Rumsey, C. L., Thomas, J. L., Thompson, K. B., Walden, A., Wang, L., Wood, S. L., Wood, W. A., Diskin, B., Liu, Y., and Zhang, X., "FUN3D Manual: 14.0," NASA TM 20220017743, NASA Langley Research Center, Hampton, VA, Dec. 2022.

[31] Thompson, K. B., Nishikawa, H., and Padway, E., "Economical Third-Order Methods for Accurate Surface Heating Predictions on Simplex Element Meshes," *AIAA SciTech 2023 Forum*, American Institute of Aeronautics and Astronautics, National Harbor, MD & Online, 2023. https://doi.org/10.2514/6.2023-2629.

[32] Thompson, K. B., O'Connell, M. D., Hinkle, A. D., and Pederson, C., "Validation of the HyperSolve CFD Solver for Entry Descent and Landing Applications," *AIAA SCITECH 2024 Forum*, American Institute of Aeronautics and Astronautics, Orlando, FL, 2024. https://doi.org/10.2514/6.2024-1973.

[33] Edwards, J., "Towards Unified CFD Simulations of Real Fluid Flows," *15th AIAA Computational Fluid Dynamics Conference*, American Institute of Aeronautics and Astronautics, Anaheim, CA, 2001. https://doi.org/10.2514/6.2001-2524.

[34] Nishikawa, H., and Liu, Y., "Third-Order Edge-Based Scheme for Unsteady Problems," *AIAA AVIATION 2018 Forum*, American Institute of Aeronautics and Astronautics, Atlanta, GA, 2018. https://doi.org/10.2514/6.2018-4166.

[35] Gnoffo, P., and White, J., "Computational Aerothermodynamic Simulation Issues on Unstructured Grids," *37th AIAA Thermophysics Conference*, American Institute of Aeronautics and Astronautics, Portland, Oregon, 2004. https://doi.org/10.2514/6.2004-2371.

[36] Nishikawa, H., "Beyond Interface Gradient: A General Principle for Constructing Diffusion Schemes," *40th Fluid Dynamics Conference and Exhibit*, American Institute of Aeronautics and Astronautics, Chicago, Illinois, 2010. https://doi.org/10.2514/6.2010-5093.

[37] Nishikawa, H., Nakashima, Y., and Watanabe, N., "Effects of High-Frequency Damping on Iterative Convergence of Implicit Viscous Solver," *Journal of Computational Physics*, Vol. 348, 2017, pp. 66–81. https://doi.org/10.1016/j.jcp.2017.07.021.

[38] "Turbulence Modeling Resource," https://turbmodels.larc.nasa.gov/index.html, Dec. 2023.

[39] Allmaras, S. R., Johnson, F. T., and Spalart, P. R., "Modifcations and Clarifcations for the Implementation of the Spalart-Allmaras Turbulence Model," *Computational Fluid Dynamics*, 2012, pp. 1–11.

[40] Spalart, P., and Allmaras, S., "A One-Equation Turbulence Model for Aerodynamic Flows," *30th Aerospace Sciences Meeting and Exhibit*, American Institute of Aeronautics and Astronautics, Reno, NV, 1992. https://doi.org/10.2514/6.1992-439.

[41] Shur, M. L., Strelets, M. K., Travin, A. K., and Spalart, P. R., "Turbulence Modeling in Rotating and Curved Channels: Assessing the Spalart-Shur Correction," *AIAA Journal*, Vol. 38, No. 5, 2000, pp. 784–792. https://doi.org/10.2514/2.1058.

[42] Menter, F. R., "Two-Equation Eddy-Viscosity Turbulence Models for Engineering Applications," *AIAA Journal*, Vol. 32, No. 8, 1994, pp. 1598–1605. https://doi.org/10.2514/3.12149.

[43] Rumsey, C. L., "Apparent Transition Behavior of Widely-Used Turbulence Models," *International Journal of Heat and Fluid Flow*, Vol. 28, No. 6, 2007, pp. 1460–1471. https://doi.org/10.1016/j.ijheatfluidflow.2007.04.003.

[44] Candler, G., Barnhardt, M., Drayna, T., Nompelis, I., Peterson, D., and Subbareddy, P., "Unstructured Grid Approaches for Accurate Aeroheating Simulations," *18th AIAA Computational Fluid Dynamics Conference*, American Institute of Aeronautics and Astronautics, Miami, Florida, 2007. https://doi.org/10.2514/6.2007-3959.

[45] McCloud, P. L., "Best Practices for Unstructured Grid Shock Fitting," *55th AIAA Aerospace Sciences Meeting*, American Institute of Aeronautics and Astronautics, Grapevine, Texas, 2017, pp. 1–14. https://doi.org/10.2514/6.2017-1149.

[46] Kleb, W. L., Park, M. A., Wood, W. A., Bibb, K. L., Thompson, K. B., and Gomez, R. J., "Sketch-to-Solution: An Exploration of Viscous CFD with Automatic Grids," *AIAA Aviation 2019 Forum*, American Institute of Aeronautics and Astronautics, Dallas, Texas, 2019. https://doi.org/10.2514/6.2019-2948.

[47] Alauzet, F., and Loseille, A., "High-Order Sonic Boom Modeling Based on Adaptive Methods," *Journal of Computational Physics*, Vol. 229, No. 3, 2010, pp. 561–593. https://doi.org/10.1016/j.jcp.2009.09.020.

[48] Loseille, A., and Alauzet, F., "Continuous Mesh Framework Part I: Well-Posed Continuous Interpolation Error," *SIAM Journal on Numerical Analysis*, Vol. 49, No. 1, 2011, pp. 38–60. https://doi.org/10.1137/090754078.

[49] Loseille, A., and Alauzet, F., "Continuous Mesh Framework Part II: Validations and Applications," *SIAM Journal on Numerical Analysis*, Vol. 49, No. 1, 2011, pp. 61–86. https://doi.org/10.1137/10078654X.

[50] Spalart, P., and Streett, C., "Young-Person's Guide Simulation Grids Detached-Eddy," NASA CR 2001-211032, NASA Langley Research Center, Hampton, VA, Jul. 2001.

[51] Prince, J. L., and Shoenenberger, M., "Independent Assessment of the Backshell Pressure Field for Mars Entry, Descent, and Landing Instrumentation 2 (MEDLI2)," NASA TM 2017-219666, NASA Langley Research Center, Hampton, VA, 2017.

[52] Alauzet, F., George, P. L., Mohammadi, B., Frey, P., and Borouchaki, H., "Transient Fixed Point-based Unstructured Mesh Adaptation," *International Journal for Numerical Methods in Fluids*, Vol. 43, No. 6-7, 2003, pp. 729–745. https://doi.org/10.1002/fld.548.

[53] Park, M. A., Kleb, W. L., Anderson, W. K., Wood, S. L., Balan, A., Zhou, B. Y., and Gauger, N. R., "Exploring Unstructured Mesh Adaptation for Hybrid Reynolds-Averaged Navier–Stokes/Large Eddy Simulation," *AIAA Scitech 2020 Forum*, American Institute of Aeronautics and Astronautics, Orlando, FL, 2020. https://doi.org/10.2514/6.2020-1139.

[54] Ekelschot, D., and Brock, J., "Enabling Metric-Based Mesh Adaptation for Advanced Compressible Flow Simulations Using US3D," *AIAA SCITECH 2022 Forum*, American Institute of Aeronautics and Astronautics, San Diego, CA, 2022, pp. 1–18. https://doi.org/10.2514/6.2022-1866.

[55] Forsythe, J. R., Hoffmann, K. A., Cummings, R. M., and Squires, K. D., "Detached-Eddy Simulation With Compressibility Corrections Applied to a Supersonic Axisymmetric Base Flow," *Journal of Fluids Engineering*, Vol. 124, No. 4, 2002, pp. 911–923. https://doi.org/10.1115/1.1517572.

[56] Simon, F., Deck, S., Guillen, P., and Sagaut, P., "Reynolds-Averaged Navier-Stokes/Large-Eddy Simulations of Supersonic Base Flow," *AIAA Journal*, Vol. 44, No. 11, 2006, pp. 2578–2590. https://doi.org/10.2514/1.21366.

[57] Carlsson, M., Davidson, L., Peng, S.-H., and Arvidson, S., "Investigation of Low-Dissipation Low-Dispersion Schemes for Incompressible and Compressible Flows in Scale-Resolving Simulations," *Computers & Fluids*, Vol. 251, 2023, p. 105741. https://doi.org/10.1016/j.compfluid.2022.105741.

[58] Pederson, C., Wood, W. A., and Hollis, B. R., "Aeroheating Predictions for a Hypersonic, Turbulent Near-Wake," *AIAA Aviation Forum 2024*, American Institute of Aeronautics and Astronautics, Las Vegas, NV, 2024. https://doi.org/10.2514/6.2024-3745.

[59] Nishikawa, H., and White, J. A., "Comparison of Two Approaches to Constructing Second- and Third-Order Nodal-Gradient Cell-Centered Finite-Volume Methods for Mixed-Element Grids," *AIAA SCITECH 2025 Forum*, American Institute of Aeronautics and Astronautics, Orlando, FL, 2025. https://doi.org/10.2514/6.2025-0071.

[60] Subbareddy, P. K., and Candler, G. V., "A Fully Discrete, Kinetic Energy Consistent Finite-Volume Scheme for Compressible Flows," *Journal of Computational Physics*, Vol. 228, No. 5, 2009, pp. 1347–1364. https://doi.org/10.1016/j.jcp.2008.10.026.

[61] Kuya, Y., Okumura, W., and Sawada, K., "A Kinetic Energy and Entropy Preserving (KEEP) Finite Volume Scheme on Unstructured Meshes for Compressible Flows," *Journal of Computational Physics*, 2023, p. 112521. https://doi.org/10.1016/j.jcp.2023.112521.

[62] Guseva, E. K., Garbaruk, A. V., and Strelets, M. K., "Assessment of Delayed DES and Improved Delayed DES Combined with a Shear-Layer-Adapted Subgrid Length-Scale in Separated Flows," *Flow, Turbulence and Combustion*, Vol. 98, No. 2, 2017, pp. 481–502. https://doi.org/10.1007/s10494-016-9769-7.

[63] Pederson, C., Oliver, T., and Moser, R. D., "An Active Model-Split for Hybrid RANS/LES of Compressible Flows," *AIAA SciTech 2022 Forum*, American Institute of Aeronautics and Astronautics, San Diego, CA, 2022. https://doi.org/10.2514/6.2022-1205.

[64] Mehta, M., Manceau, R., Duffal, V., and De Laage De Meux, B., "An Active Hybrid Reynolds-averaged Navier–Stokes/Large Eddy Simulation Approach for Gray Area Mitigation," *Physics of Fluids*, Vol. 35, No. 12, 2023, p. 125116. https://doi.org/10.1063/5.0174381.

[65] Catris, S., and Aupoix, B., "Density Corrections for Turbulence Models," *Aerospace Science and Technology*, Vol. 4, No. 1, 2000, pp. 1–11. https://doi.org/10.1016/S1270-9638(00)00112-7.

[66] Waligura, C. J., Couchman, B. L., Galbraith, M. C., Allmaras, S. R., and Harris, W. L., "Investigation of Spalart-Allmaras Turbulence Model Modifications for Hypersonic Flows Utilizing Output-Based Grid Adaptation," *AIAA SciTech 2022 Forum*, American Institute of Aeronautics and Astronautics, San Diego, CA, 2022. https://doi.org/10.2514/6.2022-0587.